ORNL/SPR-2022/2430

Clean Condensing Gas Furnace

Zhiming Gao
Kyle Gluesenkamp
Anthony Gehl
Josh Pihl
Dino Sulejmanovic
Mingkan Zhang
Tim LaClair
Kashif Nawaz
Yuxuan Zhang
Shuo Qian
Weiwei Yang
Zili Wu

March 2022

OAK RIDGE National Laboratory

ORNL IS MANAGED BY UT-BATTELLE LLC FOR THE US DEPARTMENT OF ENERGY

DOCUMENT AVAILABILITY

Reports produced after January 1, 1996, are generally available free via OSTI.GOV.

Website www.osti.gov

Reports produced before January 1, 1996, may be purchased by members of the public from the following source:

National Technical Information Service
5285 Port Royal Road
Springfield, VA 22161
Telephone 703-605-6000 (1-800-553-6847)
TDD 703-487-4639
Fax 703-605-6900
E-mail info@ntis.gov
Website http://classic.ntis.gov/

Reports are available to US Department of Energy (DOE) employees, DOE contractors, Energy Technology Data Exchange representatives, and International Nuclear Information System representatives from the following source:

Office of Scientific and Technical Information
PO Box 62
Oak Ridge, TN 37831
Telephone 865-576-8401
Fax 865-576-5728
E-mail reports@osti.gov
Website https://www.osti.gov/

ORNL/SPR-2022/2430

Building and Transportation Science Division

CLEAN CONDENSING GAS FURNACE

Zhiming Gao
Kyle Gluesenkamp
Anthony Gehl
Josh Pihl
Dino Sulejmanovic
Mingkan Zhang
Tim LaClair
Kashif Nawaz
Yuxuan Zhang
Shuo Qian
Weiwei Yang
Zili Wu

March 2022

Prepared by
OAK RIDGE NATIONAL LABORATORY
Oak Ridge, TN 37831
managed by
UT-BATTELLE LLC
for the
US DEPARTMENT OF ENERGY
under contract DE-AC05-00OR22725

CONTENTS

LIST OF FIGURES

LIST OF TABLES

ABSTRACT

Natural gas furnaces are the most common space heating equipment in the U.S. residential and commercial building markets. However, current residential natural gas condensing furnaces generate substantial acidic condensate as well as significant emissions of sulfur oxides (SOx), nitrogen oxides (NOx), carbon monoxide (CO), hydrocarbons (HC), and methane (CH_4) contributing to environmental degradation of air, water, and soil. This report describes a novel solution to reduce the environmental impact of natural gas condensing furnaces based on the technology of a monolithic acidic gas reduction (AGR) catalyst for SOx trapping, NOx redox to nitrogen, and oxidation of formic acid, CO, HC, and CH_4. The AGR technology offers the following benefits: (1) a neutral furnace condensate with a pH of ~7, allowing its safe release into the sewer system thus eliminating a second drainage system; (2) trapping and removing nearly all SOx emissions; (3) NOx emissions nearly at nearly 1-2 ng/J, more than 95% lower than new emissions standards in California; (4) the use of a low-cost heat exchanger as a condensing heat exchanger (HX) since the condensate is not acidic, avoiding the need for expensive stainless steel alloys; and (5) unburnt fuel energy recovery to boost efficiency.

The AGR component and AGR-enabled furnace performance were broadly tested to determine their effects on long-term reliability and durability, as well as SOx storage and regeneration activity. The AGR regeneration does not impair the performance in achieving neutral condensate and ultra-low NOx emissions, and the AGR catalyst subjected to regeneration activities continued to function well and achieved slightly better annual fuel utilization efficiency (AFUE). The 400-hour reliability and durability test of the retrofitted condensing furnace with the AGR component shows that the furnace unit still achieves a neutral furnace condensate with a pH of ~7 and enables 0~3 ng/J of NOx emissions. However, the 400-hour operation slightly degraded the AFUE because of soot particle accumulation caused by frequent incomplete combustion owing to inappropriate condensate drainage during testing. Thus, proper condensate drainage is critical for AGR-enabled furnaces. Furthermore, neutron computed tomography was employed to survey the aged AGR component and demonstrate high-resolution 2D and 3D representations for the nondestructive diagnosis of the AGR component. The tomography showed that the AGR component did not deform or suffer broken AGR channels.

A new AGR catalyst with low precious metal loading was preliminarily explored to identify a pathway of optimizing AGR material loading and maximizing acidic gas reduction at low cost. The new AGR component can reduce precious metal loading by 38% and still achieve neutral condensate and ultralow NOx emissions. The furnace with the AGR component of low Pt/Rh loading enables a maximum AFUE of 97%, which is meaningfully higher than the original furnace. Long-duration testing for the furnace enabled with the low precious metal loading AGR component will be vital in future research.

Although the current work demonstrates a proof of concept for the AGR-enabled furnace, the AGR assembly needs to be optimized and integrated into the design of new OEM furnace products. Furthermore, the AGR technology can be applied not only for residential gas furnaces, but also for commercial rooftop units, gas heat pumps, gas-fired water heaters, combustion boilers, and other systems.

1. INTRODUCTION

1.1 Problems of Residential Furnaces

The U.S. has more than 118 million homes and 5.5 million commercial buildings. Approximately 47 million U.S. households use natural gas furnaces as their main heating source. U.S. Energy Information Administration (EIA) data indicate that 43% of residential energy (equivalent to 2.62 quadrillion BTUs) is consumed by space heating in the United States [1]. Improved efficiency and performance of residential gas furnaces is vital for achieving energy savings, reducing greenhouse gas emissions, and meeting the stringent regulatory requirements for pollutant emissions [2].

Prior to the 1980s, representative residential furnaces achieved an annual fuel utilization efficiency (AFUE) of only 60% [3]. An effective approach for improving furnace efficiency is to decrease the temperature of the combustion exhaust or flue gas by using a low-cost heat exchanger (HX) to preheat cold air for space heating. However, sulfur, nitrogen, and carbon, which typically exist in natural gas or its combustion products, form acidic gases (e.g. SO_3, SO_2, NO_2, NO, formic acid, etc.) in the flue gas. Once the flue gas cools below the dew point of its constituents, the acidic gases condense and combine with water present in the combustion products to produce acidic solutions that cause corrosion and fouling problems. The first condensation corrosion in furnaces was reported as early as 1901 [4]. The acid dew point of SO3 could be as high as 115-150°C under natural gas combustion conditions. Two strategies are typically used to avoid corrosion and fouling due to acid condensation: (1) maintaining the exhaust above the dew point temperature, which limits the maximum furnace efficiency; or (2) using corrosion-resistant stainless-steel alloy materials to construct HXs, which results in a significant cost penalty. Non-condensing furnaces adopt the former strategy, and most U.S. homes still use non-condensing units with an AFUE of about 80% or less due to the release of flue gas at temperatures exceeding 160°C to the outdoor environment [5]. Up-to-date condensing furnaces employ the latter technology and achieve more than 90% AFUE by capturing the latent heat from the condensing vapor and reducing flue temperature to less than 40°C while avoiding the corrosion and fouling issues [6]. The corrosion-resistant stainless-steel alloys are ferritic stainless-steel alloys with a high chromium and molybdenum content, as the high chromium content provides general corrosion protection, and the molybdenum provides resistance to pitting corrosion that can occur in stainless steels [3]. Condensing furnaces are expensive compared to non-condensing units. Lutz et.al. [7] and Lekov et.al. [8] reported that condensing furnaces' payback time could be more than ten years. The market penetration of condensing furnaces is limited by a higher furnace cost and expensive installation and maintenance costs.

1.2 Current Studies on Residential Furnaces

Various studies were carried out to extend the market penetration of high efficiency condensing furnaces to replace old inefficient residential furnaces, including component optimization, low-carbon fuels, system innovation . In the component optimization, Wu et.al. [9] carried out CFD to optimize and accelerate the chamber design of next-generation gas furnace in reducing the cost and development cycle. Tu et.al. [10] assessed the effects of furnace chamber shape on the moderate or intense low-oxygen dilution combustion. Belosevic et.al. [11] presented experimental investigation and modeling of flow and heat transfer processes in a household furnace, showing considerable energy savings. Yin et.al. [12] reported the impact of duct flow resistance on residential heating energy use in systems with various blowers. For low-carbon fuels, Zhao et.al. [13], Omari et.al. [14], and Jiru et.al. [15] explored the influence of renewable biogas, hydrogen, and biofuels on the performance of a residential furnace. Chandrasekaran et.al. [16], Kakareka et.al. [17], and Tashtoush et.al. [18] characterized and compared emissions in residential furnaces using various alternative fuels. In the system innovation, Addo–Binney et.al. [19] developed an integrated system consisting of a natural gas furnace and a heat pump, showing significant reductions in energy consumption, greenhouse gas emissions, and operating cost. Gluesenkamp et.al. [20] and Abu-Heiba et.al. [21] proposed

a self-powered condensing furnace that imports no electricity, i.e. a power cycle integrated into the furnace generates all the electrical power needed, and the heat rejected by the power cycle contributes to space heating. Elias et.al. [22] showed that upgrading old non-condensing residential furnaces with high-efficiency condensing units is beneficial in reducing both heating expenses and carbon emissions. Milcarek et.al. [23] introduced a residential furnace integrated with a micro-tubular SOFC stack to create a micro-CHP system in exploring high efficiency.

However, these emerging furnace technologies inevitably generate substantial acidic condensate, as well as NOx, CO, HC, and methane emissions, exaggerating long-term environmental issues related to soil, water, and air. California is enacting new standards for residential and commercial furnace emission levels (14 nanograms/joule (ng/J) or less), to limit the amount of NOx emissions released into the air [24]. U.S. EPA regulations require 40 ng/J of NOx or less. Acidic condensate removal and treatment has also been identified as an issue related to greater installation and maintenance costs. The combination of a higher furnace cost and expensive installation and maintenance costs limits the market penetration of condensing furnaces. All these issues are a direct result of the acid content in the natural gas combustion exhaust. Consequently, to develop ultra-clean and efficient condensing furnaces while reducing the furnace's capital cost as well as reducing installation and maintenance cost related to acidic condensate treatment, a novel acidic gas reduction (AGR) catalyst can play a critical role. Advanced catalysts for acidic gas trapping and reduction have been successfully and widely applied in automobile emissions control [25, 26]. The innovative AGR technology is capable of substituting less expensive materials for the high alloy stainless steels used in current condensing heat exchangers, as well as the reduction of installation and maintenance costs. Developing a low-cost AGR using acidic gas trapping and reduction technologies is a feasible pathway to make furnaces more efficient, simpler and less expensive. Based on the authors' knowledge, there is not currently or previously existing AGR technology for the condensing furnace application.

1.3 AGR Diagnostics using Neutron Computed Tomography

With high penetration power through most metal materials, neutron imaging has been widely used to nondestructively image internal features such as porosity [27], cracks [28], species distribution within batteries, catalysts [29, 30], particle filters [31, 32], fuel cells [33, 34], fundamental heat and mass transfer [35, 36], and many other materials and components [37, 38]. Neutron computed tomography (NCT) is a powerful imaging technique that leverages the high scattering cross section of neutrons for light elements to generate hundreds of 2D projections over 180° or 360° rotation as raw data and then reconstructs a 3D virtualization with the integration of the 2D images after correcting saturated pixels and background noise. This makes NCT well suited to nondestructively survey the spatial distribution within the AGR component and to help understand the AGR aging process in furnace operation. In the project, the AGR-enabled condensing furnace was in operation for approximately 400 hours to test the reliability and durability of the retrofitted unit and the AGR component. The observation revealed that long-term operation degrades the AFUE performance of the AGR-enabled furnace slightly for cases with high heating capacity. Upon removing the aged AGR from the furnace unit, accumulated soot particles were found on the metal net mounted in the AGR's inlet cone zone, but significantly less soot was found in the AGR's outlet cone zone. However, this disassembly process is destructive, so studying the internal state of the AGR during operation or after disassembly is impossible. Thus, NCT can be used to demonstrate 3D diagnosis and mapping of such as soot particle loading or aging distribution within the full-size AGR component. The results can provide an in-depth view inside the AGR component with spatially resolved structural and particulate distribution information. The in-depth view and comprehensive analysis that NCT enables could improve real AGR component design and enhance the efficiency and emissions control of future novel natural gas condensing furnaces that use AGR. Based on the authors' knowledge, there is not previously existing NCT applications for real heating, ventilation, and air conditioning (HVAC) commercial components and systems such as AGR and furnace.

1.4 Project Objective

The project aims to develop a cost-effective AGR catalyst component which allows a new condensing natural gas furnace with ultra-clean flue gas emissions and neutral condensate. The novel AGR-enabled condensing gas unit aims to achieve an effectiveness of approximately 100% for SOx trapping removal, more than 95% for NOx redox, and oxidation of formic acid, CO, HC, and CH_4 oxidation, leading to neutral condensate [39]. The neutral condensate enables the potential of a simpler and less expensive furnace design and installation. The report describes the development of the AGR component, a prototype of an AGR-enabled furnace, as well as evaluation of the AGR-enabled furnace performance over various operating conditions including a 400-hour long-term test. NCT is further used to provide an in-depth view inside the AGR component before and after the 400-hour long-duration test. The report also address the exploration of new AGR enabling with low precious metal loading. In addition, the report addresses furnace condensate acidity and chemistry analysis, as well as its impact on alloy corrosion.

2. AGR METHODOLOGY AND FURNACE EXPERIMENTAL SETUP

2.1 AGR Component and AGR-Enabled Condensing Furnace

Figure 1 shows the AGR catalyst sample which was fabricated based on a monolithic substrate washcoated with TiO_2 Anatase, CuO and a small amount of Platinum (Pt). The key chemical reaction mechanism of SOx trapping removal, NOx redox to N_2, and CO/HC/CH_4/formic gas oxidation is also displayed in Figure 1. The key material composition recipe is listed in Table 1. In the authors' lab benchmark reactor tests with the small sample size that is 2 cm diameter by 5 cm long, the results have shown that the catalyst sample enables not only adsorption of SOx, NOx redox to N_2, but also oxidation of CO, hydrocarbons (including formaldehyde) and methane. In the benchmark reactor tests at 250°C, 100% of CO is oxidized to CO_2. A regeneration approach for the AGR catalyst was also demonstrated to restore the catalyst capacity for SOx following extensive SOx trapping.

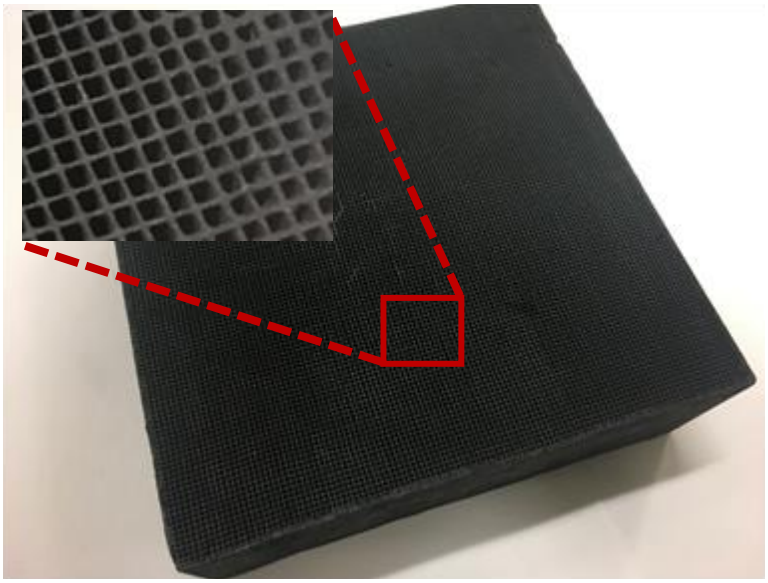

SOx adsorption
$SO_2+0.5O_2 \Rightarrow SO_3$
$SO_3+TiO_2\text{-}A \Rightarrow TiO_2\text{-}A \cdot SO_3$
NOx redox to N_2
$NO+CO \Rightarrow CO_2+0.5N_2$,
$NO_2+2CO \Rightarrow 2CO_2+0.5N_2$
CO/HC/CH_4/formic gas oxidation
$CO+0.5O_2 \Rightarrow CO_2$,
$C_3H_6+4.5O_2 \Rightarrow 3CO_2+3H_2O$,
$CH_4+2O_2 \Rightarrow CO_2+2H_2O$
$CH_2O+O_2 \Rightarrow CO_2+H_2O$

Figure 1: A sample of AGR catalyst and reaction mechanism

Table 1: The material composition of AGR catalyst

Cell density		400 cpsi
Materials & composition	TiO_2 loading	195 g/L (Anatase TiO_2)
	Cu loading	24.4 g/L
	Pt loading	4.27 g/L (Pt only)
TiO_2 surface area		50 m^2/g

The full-size AGR component fabrication and assembly are shown in Figure 2(a) and 2(b). The prototype component consists of a 2-liter shell canister and accessory parts in addition to the monolith catalyst. A non-toxic silica fiber mat is added between the shell canister and catalyst to fix the catalyst to the shell and avoid any vibration. Two connection cones (i.e., a divergent and convergent cone) are used to connect the shell canister and monolith catalyst with the accessory parts. In addition, a metal net mounted in each cone is used to enhance the mixing effect of flue gas and prevent the horizontal movement of the catalyst. Other

accessory parts include several elbows, tubes and bolted flange clamps, which are used to connect the AGR component to the furnace HXs (see Figures 2(c) and 2(d)). As shown in Figure 2(c), the bolted flange clamps allow easy replacement of the catalyst component while the holes along the horizontal tubes are used for attachment to the primary HX tubing of the natural gas furnace. This design aims to meet the need for repeated catalyst monolith installation and disassembly. Figure 2(e) shows a prototype 2-liter AGR-enabled condensing furnace which was retrofitted to a commercial non-modulating condensing furnace with a nameplate rating of 23.4 kW (80 kBTU/h) and 92% AFUE.

The retrofit also included a condensing HX with an enhanced surface. To minimize overall furnace configuration variation and avoid OEM manufacturing cost increment, we adopted a cost-effective approach of modifying the secondary HX to increase its heat transfer surface without altering the component's overall geometry and space size. Figure 3 displays the modified secondary HX with the enhanced heat transfer surface. In the modification, two row heat transfer surfaces were add in the HX. The screwed metal implemented in the tubes are used to enhance heat transfer.

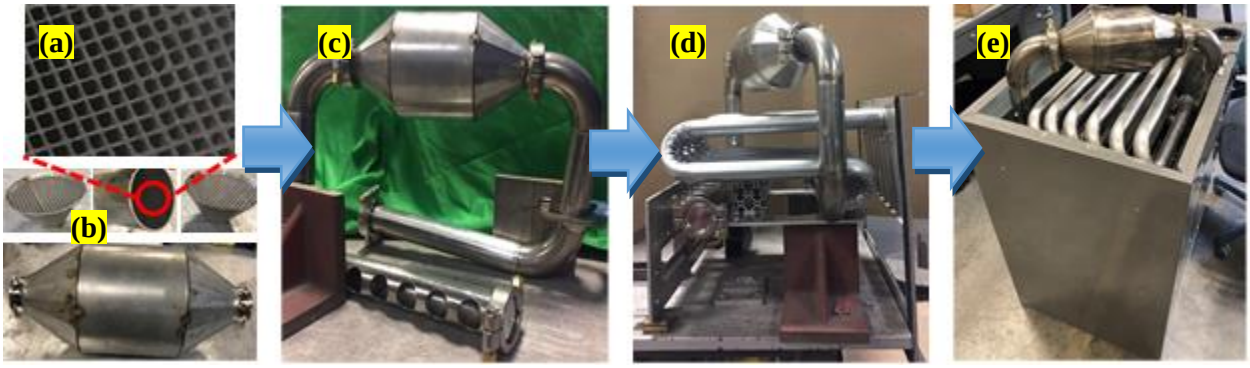

Figure 2: AGR-enabled condensing furnace retrofitted to a commercial 23.4 kW (80 kBTU/h) condensing furnace; (a) AGR catalyst; (b) AGR housing; (c) overall AGR component and accessory parts; (d) AGR integration with furnace primary HX; € a prototype AGR-enabled furnace.

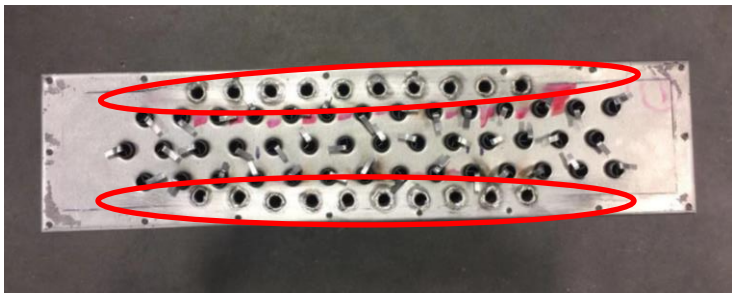

(a) Side review

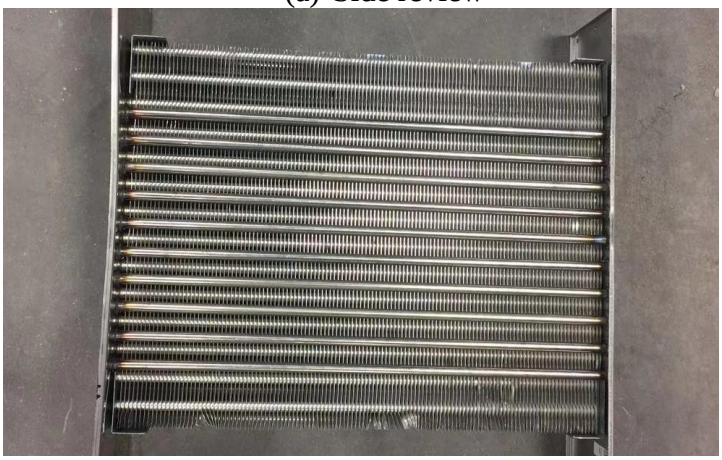

(b) top view

Figure 3: The modified secondary HX; (a) shows side view; (b) shows top view; the new added heat transfer tubes is marked in the red color.

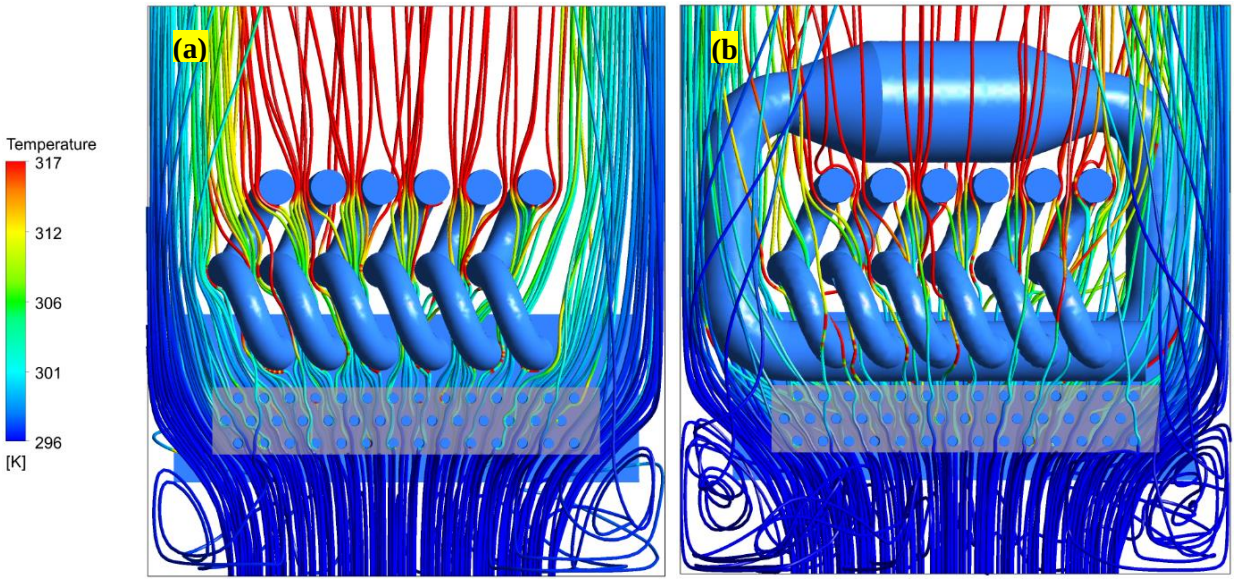

Figure 4: Comparison of furnace heating-air flow patterns with or without the AGR component; (a) a baseline furnace; (b) the retrofitted furnace integrated with AGR.

The AGR assembly and integration design deliberately consider the configuration and HX size of the natural gas furnace with the integration of AGR component to minimize the cost penalty added to the new furnace. In addition, a computational fluid dynamics simulation was carried out by using Ansys Fluent to evaluate the AGR integration on furnace flow patterns and heat transfer performances [40]. Figure 4 shows the simulated heating-air flow movement inside the furnace with AGR component. The simulation assumptions for furnace configuration, geometric size, flow rates and temperatures used in the simulated furnace are measured from the tested furnace. Although the AGR component can alter heating-air flow movement, the results show that the pressure drop due to AGR component is very small, indicating limited impact of AGR component on overall heating-air flow performance. Please note that the prototype aims to demonstrate proof of concept for the AGR-enabled furnace performance and the optimization of commercial product is not the scope of current study. The authors acknowledge that there is a significant optimized space for the AGR assembly and integration in the potential design of OEM new furnace products.

2.2 Furnace Experimental Setup

The furnace experimental setup and testing procedure followed the requirements for instruments and testing provided in ANSI/ASHRAE Standard 103-2017 [41]. Figure 5(a) shows the testing system for the AGR-enabled condensing furnace which was set up in a furnace testing chamber. In the experimental testing system, a vertical supply test plenum was installed above the furnace unit. An extended casing and horizontal vent pipe with the same cross-sectional area as the vent pipe is connected to the furnace flue gas exit above the top of the furnace. The key work during the experimental setup included (1) adding an electrical power meter; (2) installing thermocouples for temperature measurement of the flue gas, supply air, and the unit jacket surface; (3) adding a natural gas flow meter; and (4) adding flue gas sample tubes.

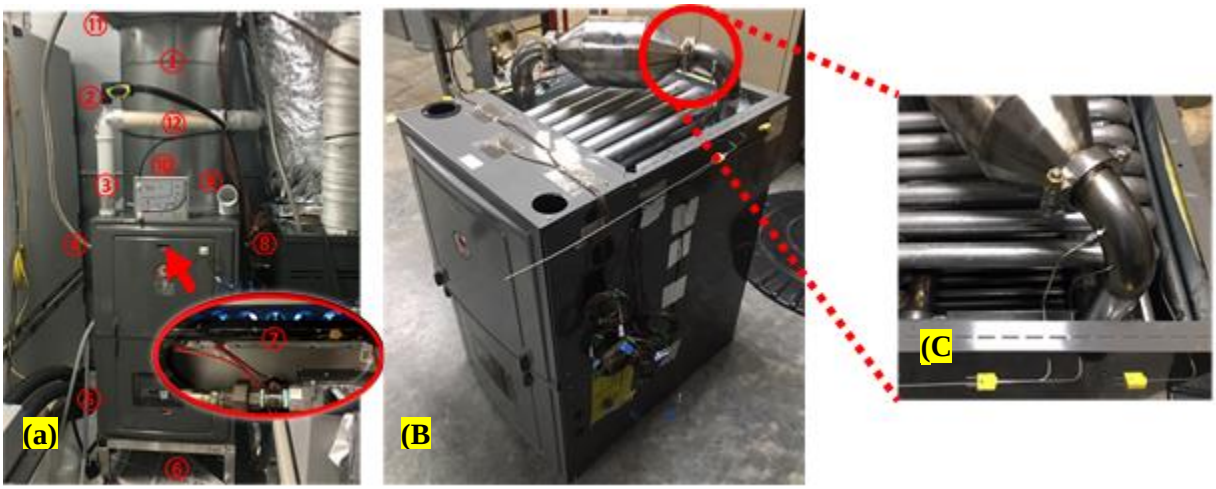

Figure 5: (a) the AGR-enabled 23.4 kW (80 kBTU/h condensing furnace testing system: (1) plenum, (2) combustion & emissions analyzer; (3) flue gas exit; (4) natural gas pipeline, (5) condensate collection, (6) returning airflow, (7) burners, (8) type-T thermocouples, (9) burner airflow, (10) manometer, (11) damper, (12) extended casing and horizontal vent pipe; (b) the AGR-enabled furnace with thermocouples; (c) the AGR flue gas sample tubes and thermocouples

The thermocouples for flue gas temperature measurement include six type-K probes for detecting high temperature flue gas variation along the unit's primary HX and the inlet and exit of the AGR. The measurement range and uncertainty of the type-K probes are 0 to 1038°C and +/- 2.8°C. Figure 5(b) shows type-K thermocouples and two gas-sampling tubes installed before and after the AGR component to measure and monitor flue gas temperature and composition. Figure 5(c) shows the details of these instruments at the exit of the AGR component. A type-T thermocouple is installed at the flue gas exit of the unit, and another type-T thermocouple is installed at 1.5m along the vent pipe after the flue gas exit from the unit. In addition, eleven type-T thermocouples are added to measure the temperature on the furnace's exterior panel surfaces, including upper and lower positions on the left- and right-side panels, front and back panels, top and bottom panels, and on the blower shell. To measure the supply heating air flow temperature in the plenum, a set of type-T thermocouples are used to construct a thermocouple grid arrangement in a test plane perpendicular to the axis of the plenum. Finally, one type-T thermocouple is used to measure returning air temperature (or room air temperature). In the testing system, a Bacharach PCA 400 combustion & emissions analyzer is used to record O_2, CO_2, CO, and NOx concentrations with the uncertainties of ±0.1%, ±0.1%, ±3 ppm, and ±3 ppm, respectively. A natural gas flow meter with the uncertainty of ±0.5% is used to directly record the fuel consumption. A manometer is used to monitor that the pressure drop of heating supply air flow is within the range required by the furnace manufacturer of 0.28-0.8 inches of water column. The temperature difference between the supply air flow and return air flow is also monitored to ensure that ΔT_{supply} is within the range required by the test standard of ANSI/ASHRAE Standard 103-2017. A Labview-based data acquisition graphical user interface (see Figure A1) was developed to automatically recorded the data at a frequency of 1.0 Hz. The condensate collection was performed manually, so it was independent from the data acquisition system. The mass error associated with the measuring instrument is not exceed ±0.1% of the quantity measured.

The entire furnace tests performed (following conditions specified in ANSI/ASHRAE Standard 103-2017) includes several steady-state cases, heat-up and cool-down tests, and cyclic tests. To accelerate testing in an optimal way, the steady-state, cool-down and heat-up cases are performed together in one test sequence, which the steady-state case is carried out first, followed by the cool-down and heat-up cases. The cyclic tests is completed in a separate sequence. The 30-minute steady-state testing starts after flue gas temperature variation in three successive 15-minute readings meets not more than 0.55°C. The steady-state testing lasts 30 minutes, and condensate is collected during the 30-minute steady-state testing. Once the steady-state testing is completed, the burner is turned off. Flue gas temperature is measured at 1.5 and 9 minutes after the burner shut off. Then the burner remains off until equilibrium conditions are achieved, which is indicated by variations in the flue gas temperature of no more than 1.7°C between 3 successive reading taken 15 minutes apart. After the equilibrium conditions are achieved, the furnace turns on. Then flue gas temperature is measured at 0.5 and 2.5 minutes after the burner comes on. In the cyclic testing, the "on" cycle duration is 3.87 minutes and "off" cycle duration is 13.3 minutes. The on or off switch operation actions is not more than 6s. The condensate is also collected during the cyclic testing. Figure 6 shows the flue gas temperature of the commercial furnace baseline for the steady-state, cool-down, heat-up tests, and cyclic tests.

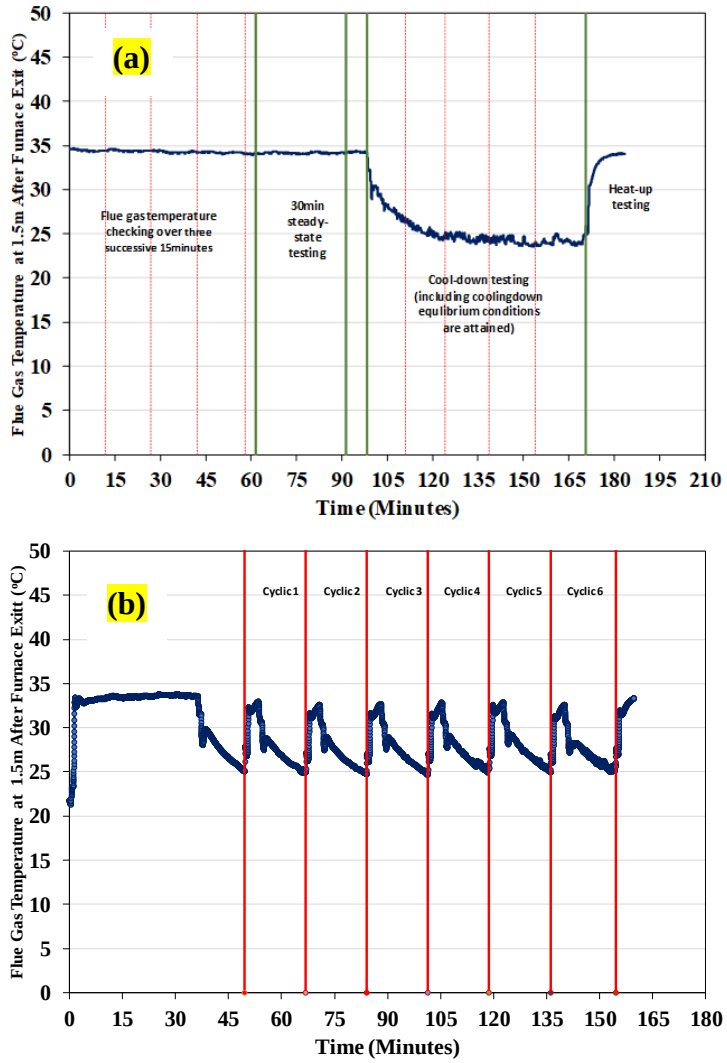

Figure 6: OEM furnace baseline testing for (a) steady-state, cool-down and heat-up tests, and (b) cyclic cases. The testing procedure follows ANSI/ASHRAE Standard 103-2017.

2.3 Flue Gas Chemistry Analysis

The flue gas used for acidity and chemistry analysis was sampled from flue gas sampling tubes shown in Figure 7. EPA Method 8 [42] is used to detect and identify any gas species that may contributing to the acidity of the condensate samples, and therefore implicated in corrosion of the heat exchanger. The EPA method can collect SO_3 (gas) and H_2SO_4 (mist) separately from the SO_2, allowing the ratio of SO_2 : sulfuric acid to be determined. Knowing both the SO_3 and SO_2 is critical because SO_2 is relatively insoluble in water and will pass through the furnace as a gas, whereas SO_3 and H_2SO_4 mist are very soluble in water and will likely condense on the secondary heat exchanger. In the test method, the flue gas is bubbled through impingers with different solutions in them that are chilled in an ice bath, and the H_2SO_4 mist is collected on a filter. The impingers are then measured to quantify the sulfur species. One of the concerns with the sampling of this furnace was that the SOx species were expected to be in very low concentration, so a long sampling period was required to accumulate enough volume of flue gas to make the measurement. Similar methods are used to accumulate enough NO2 and other acidic gases.

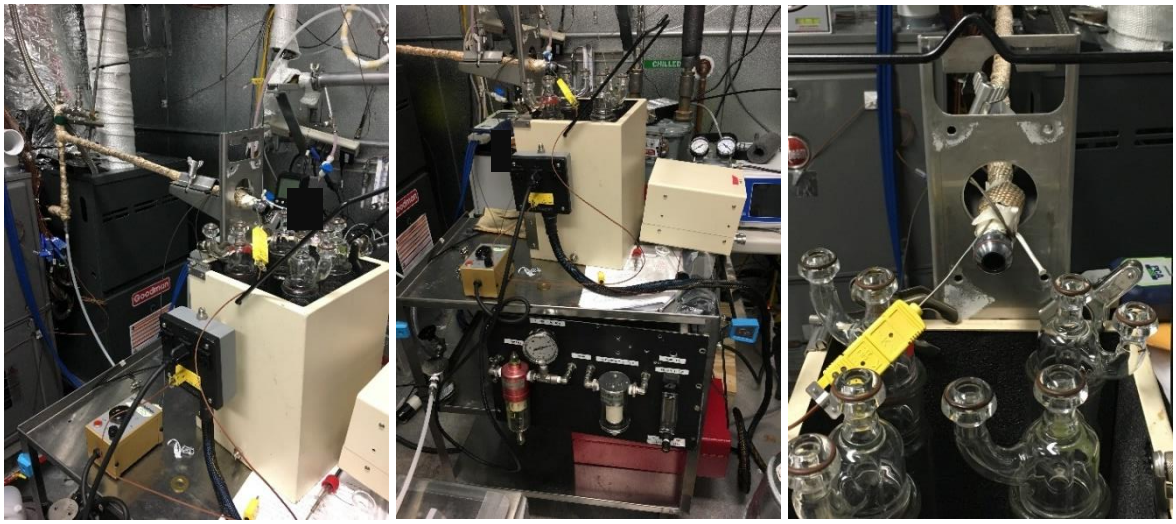

Figure 7: EPA method 8 for gas sampling.

2.4 Corrosion Tests with Acidic Condensate

Corrosion testing of alloy samples was done using a 1-inch Gamry isolation apparatus (see Figure 8 below). The tested alloy is first placed on a flat wooden stage and is secured to the Gamry isolation apparatus by a metal clamp. The bottom of the Gamry isolation apparatus is made of Teflon, which seals the one-inch diameter area of the alloy. This allows for containment of the liquid inside the apparatus. The acidic condensate of the furnace is added to the Gamry isolation apparatus with the top covered. The alloy surface is exposed to the condensate liquid for a minimum of 500 hrs. After the exposure, the alloy is dissected, and metallography studies are done to determine the depth of corrosion. SEM imaging and EDS analysis are performed to determine the corrosion products on the surface of the alloy.

In the detailed corrosion testing, a section of the condenser pipe (see Figure 8(a)) was cutout from the primary heat exchanger of the tested furnace; the pipe was first cut along the flow direction (see Figure 8(b)), and then was unrolled to form a flat test section (see Figure 8(c)). A circular area of the sample with 2.0 cm diameter was used for exposure to condensate liquids, as shown in Figure 8(d). The yellow tape isolates the exposure area from the rest of the plate. Figure 8(e) shows more tape to make sure the liquid only contacts the circular area of the metal sample. In Figure 8(f) and 8(g), a clamped Gamry paint cell is placed over the area that is to be exposed. 100 mL of the condensate was added to the Gamry isolation apparatus with the top covered. Then the metal surface was exposed to the condensate liquid over a minimum of 500 hrs.

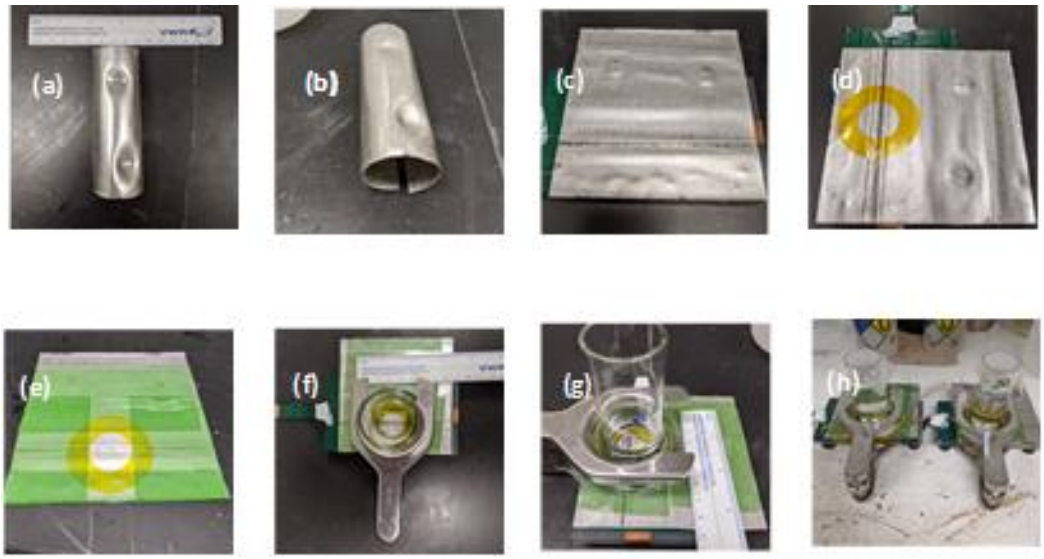

Figure 8: Metal sample and corrosion testing.

2.5 Demonstration of the AGR Regen Strategy

The proposed AGR component is capable of continuous SOx trapping until it is saturated. Typical sulfur concentrations in the natural gas pipeline are low, and a furnace has to run several years to degrade the AGR SOx trapping capability. Thus, an off-line method for AGR component SOx trapping and regen was adopted in the study. Figure 9 shows the full-scale SO2 trap experiment setup, which allows the AGR component removed from the new furnace to carry out its regeneration in an offline regen reactor.

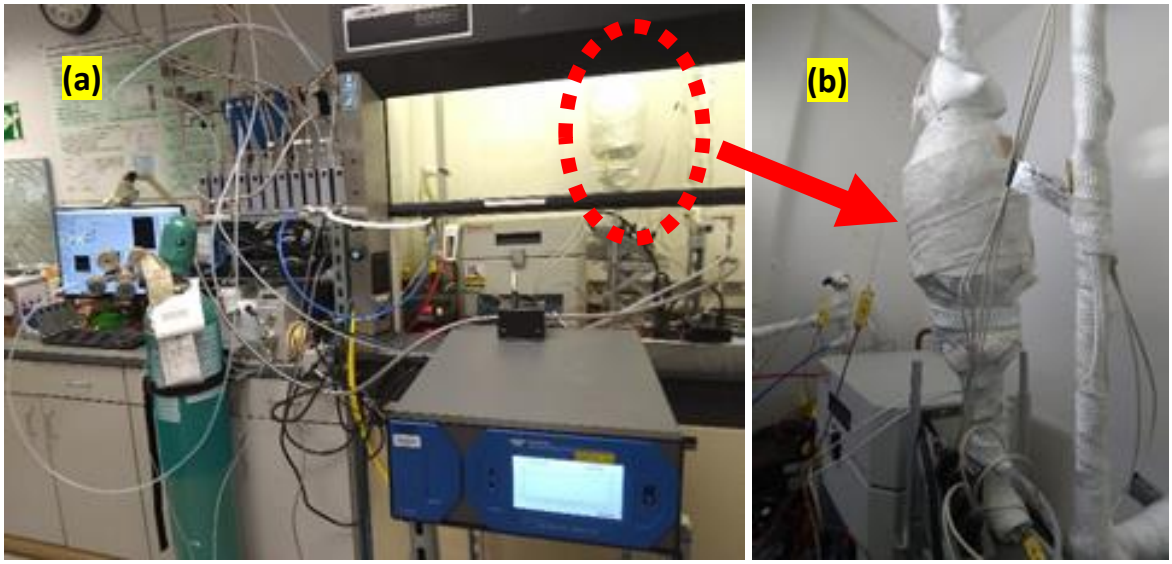

Figure 9: SO_2 full scale trap experiment setup; (a) the entire flow reactor system; (b) a close-up of the full-size trap wrapped in insulation.

In the demonstration, a full-size 2-liter AGR catalyst sample was regenerated under synthetic furnace exhaust conditions of 4% H_2, 13.6% H_2O, and a balance of N_2 (82.4%) at 250°C after completing a trapping testing case with elevated SOx exposure. 100ppm SO_2 was considered in the trapping to accelerate SOx trapping process because SOx concentration from furnace flue gas is typically less than 1ppm. The synthetic furnace exhausts for SOx trapping consists of 6.7% O_2, 8.0% CO_2, 13.6% H_2O, 66.7PPM C_3H_8, 200 PPM CO, 20PPM NO, and a balance of the rest of N_2 besides 100PPM SO_2. The testing space velocity is 3000/hour.

2.6 Annual Fuel Utilization Efficiency (AFUE) Analysis tool

An AFUE analysis tool for residential furnaces was developed by following ANSI/ASHRAE Standard 103-2017. The analysis is a complex method based on the furnace configuration and specific components equipped, as well as detailed furnace testing and measurement data. This tool includes three worksheets: unit and configuration selection (see Figure A2); geometry and measurement data input (see Figure A3); and AFUE and key results (see Figure A4). The tool can be used to estimate the AFUE of both condensing and non-condensing furnaces with single-stage, two-stage, and step-modulating functions. The tool has been validated with experimental data from ORNL other commercial natural gas furnaces, including a 11.7 kW (40 kBTU/h) two-stage condensing furnace and a 23.4 kW (80 kBTU/h) non-modulating non-condensing furnace. The AFUE of the condensing furnace was rated at 96% while the tool evaluated a value of 95.9%. The AFUE of the non-condensing furnace was rated at 80% while the tool evaluated 84.0%. The results indicate the tool is reasonably accurate in the evaluation of new R&D modified furnace unit.

3. CONDENSATE ACIDITY AND CORROSION TESTS

3.1 Acidic Content Tests of Baseline Furnace

The original non-modulating condensing furnace with a nameplate rating of 23.4 kW (80 kBTU/h) and 92% AFUE was tested as a baseline for comparison to later tests of the furnace as retrofitted with the prototype AGR component. The furnace testing followed ANSI/ASHRAE Standard 103-2017. In the tests, condensate and sampled flue gas emissions were collected at various heating capacity. Table 2 summarizes the acidity analysis of the condensate samples collected. The measured pH value varied within the range of 3.42-3.76 while the measured formate concentration was 9-14 ppm. The test employed detects sulfate, nitrate, formate, acetate, and chlorine anions. However, both the sulfate and nitrate concentrations were very limited, with measured levels below the instrument resolution of 2 ppm, so it was not possible to detect the precise sulfate and nitrate levels. The detection of formate ion as the dominant species in the condensate is of particular interest for corrosion. Formic acid aggressively attacks steel, including stainless steel.

Table 2 Acidic analysis for condensate samples

Heating capacity	Condensate pH	Formate	Sulfate	Nitrate
80,000 BTU/h	3.42	14ppm	<2ppm	<2ppm
80,000 BTU/h	3.55	9ppm	<2ppm	<2ppm
65,000 BTU/h	3.76	-	-	-

To better characterize and understand the acidic gas concentrations in the flue gas, flue gas sampling was carried out using EPA method 8. The results from the measurements are shown in Table 3. The flue gas sampling data were collected from upstream of the furnace condenser operating at 19.1 kW (65,000 BTU/h) and 23.4 kW (80,000 BTU/h) heating capacity. Each flue gas sampling covered more than five hours of furnace operation and nearly 2000 liters of flue gas samples were collected. The analyzed results revealed that the flue gas concentration of SO_3/H_2SO_4 mist was no more than 0.57 µg/Liter-flue gas, whereas the SO_2 concentration was 1.14 ~ 1.41 µg/Liter-flue gas, resulting in a SO_2/SO_3 ratio of >2.0, during the furnace operations. In addition to SOx species, there was interest in determining concentrations of formaldehyde in the gas phase since formic acid had been identified in the condensate. Formaldehyde is a common combustion product of natural gas, and formic acid is a partial oxidation product of formaldehyde. Measurement during 23.4KW (80,000 BTU/h) heating capacity conditions showed a formaldehyde concentration of 10 ppm in the flue gas.

Table 3 Chemistry analysis for flue gas samples

Heating capacity	SOx	SOx as SO_3	SOx as SO_2	Nitrate	Formate
Heating capacity	µg/L-flue gas	µg/L-flue gas	µg/L-flue gas	µg/L-flue gas	µg/L-flue gas
80,000 BTU/h	1.71	<0.57	1.14	<0.57	1.43
65,000 BTU/h	1.98	<0.57	1.41	0.750	0.37

3.2 Corrosion Tests with Baseline Furnace Acidic Condensate

Because of considerable acidity (3 ~ 4 pH) of the condensate liquid, corrosion experiments were carried

out with the condensate and alloy tubes cut from the heat exchanger of the condensing furnace. The condensate of the furnace was collected at two different heating outputs: 19.1 kW (65,000 BTU/h) and 23.4 kW (80,000 BTU/h). In the 500-hour corrosion test, the alloy was exposed to the condensate liquid. The alloy was dissected after the exposure, and metallography studies were carried out to determine depth of corrosion. The figures below are the preliminary results showing high resolution optical images from metallography. Figure 10(a) shows a cross section of the unexposed cutout of the metal pipe used in the furnace primary heat exchanger. Figure 10(b) shows a cross section of the sample exposed to 65,000 BTU/h condensate solution (pH=2.94). Figure 10(c) shows a cross section of the sample exposed to 80,000 BTU/h condensate solution (pH=3.07). The results clearly show visible damage to the galvanized coating layer of metal after 500 hours of exposure. Therefore, it is confirmed that the acidic furnace condensate solution damages the protective layer of the furnace heat exchanger metal pipes. Here the pH values of the condensate samples are slightly different from Table 2 due to the usage of different instruments and collection timing, but still stay within a reasonable deviation.

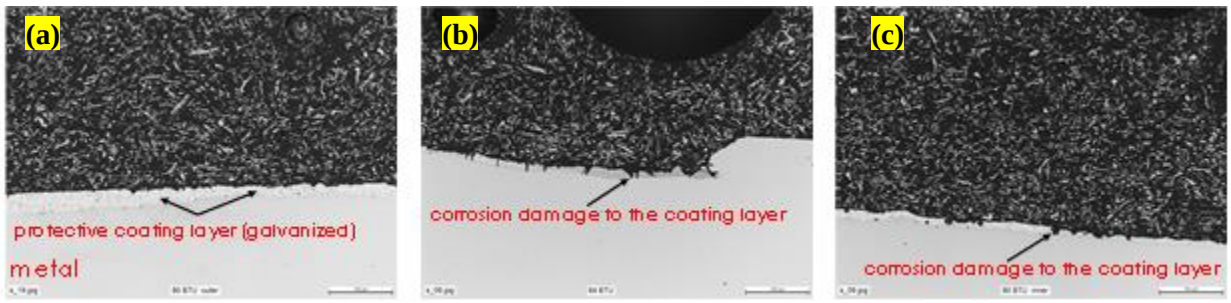

Figure 10: Corrosion testing analysis of alloy materials with condensate from various heating capacity scenarios; (a) original protective coating layer; (b) corrosion damage with 65 kBTU/h condensate; (c) corrosion damage with 80 kBTU/h condensate

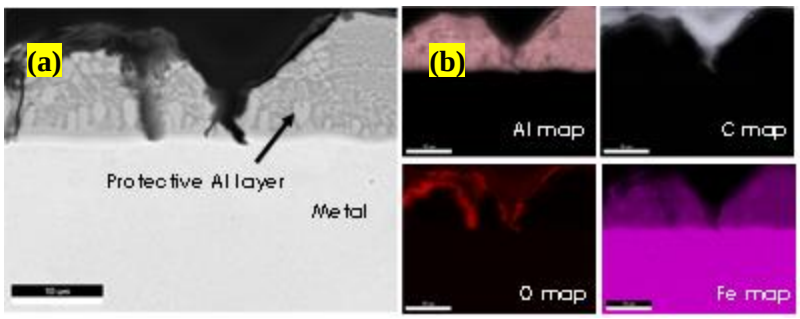

Figure 11: SEM image on (a) protective AL layer and (b) elemental mapping.

Detailed scanning electron microscope (SEM) images with elemental mapping were also analyzed for the metal samples after they completed the 500-hour corrosion tests using the condensate collected from the condensing furnace operating at 65,000 BTU/h. The results are shown in Figures 11. The images show that aluminum forms a protective layer but it is clear that the protective layer is damaged (see Figure 11(a)). The oxygen map (see Figure 11(b)) shows that oxygen species are entering and creating crevices in the protective layer of the metal. The spectra of elements detected by the SEM-EDS instrument show that the major elements are Al and Fe. It is believed that small organic acids are the corrosive compounds, which corrode the metal surface. The results provide in-depth understanding of the alloy compatibility with the condensate solution.

4. AGR-ENABLED FURNACE TESTS

4.1 Fresh AGR-Enabled Furnace Tests

The retrofitted condensing furnace with the fresh AGR was tested over various gas input ratings ranging from 17.6 kW (60,000 BTU/h) to 23.4 kW (80,000 BTU/h). During all the tests, condensate samples were collected from both cold start and steady-state cases. Figure 12(a) shows a comparison of condensate acidity of the retrofitted AGR-enabled furnace with the original OEM furnace. The steady-state data confirm that the pH of the collected condensate at >22.0 kW (>75 kBTU/h) cases is slightly above 7 while the pH of the condensate collected from the OEM furnace is 3-4. This indicates that the AGR device removes more than 99.9% of acidic content from the condensate. In the cold-start cases, the results show that the pH of the collected condensate is 6.3-6.5, which is slightly less than the steady-state data. The cold-start results still reveal that more than 99.9% of the acidic content from the condensate is reduced by the AGR. Inductively Coupled Plasma (ICP) analysis, a powerful chemical analysis method, was used to identify both trace amounts and major concentrations of all elements used in the AGR catalyst. The results show no detectable metals by ICP in all the condensate samples. This indicates that the AGR material and component is stable and reliable.

The impact of AGR on NOx reduction is shown in Figure 12(b). Compared to 35-40 ng/J of NOx emissions from the original OEM furnace without the AGR, the AGR-enabled furnace emits 1-2 ng/J of NOx. Thus, the AGR reduces the NOx emissions by more than 95% in the furnace. New California state regulations for residential and commercial furnace emission require all furnaces installed as of October 2019 to meet 65% lower NOx emissions (from 40 to 14 ng/J or less) (Liberty 2020). Compared to the 14 ng/J limits under the new standards, the furnace integrated with AGR provides approximately 90% lower NOx emissions, achieving an ultra-clean flue gas while simultaneously enabling an eco-friendly condensate.

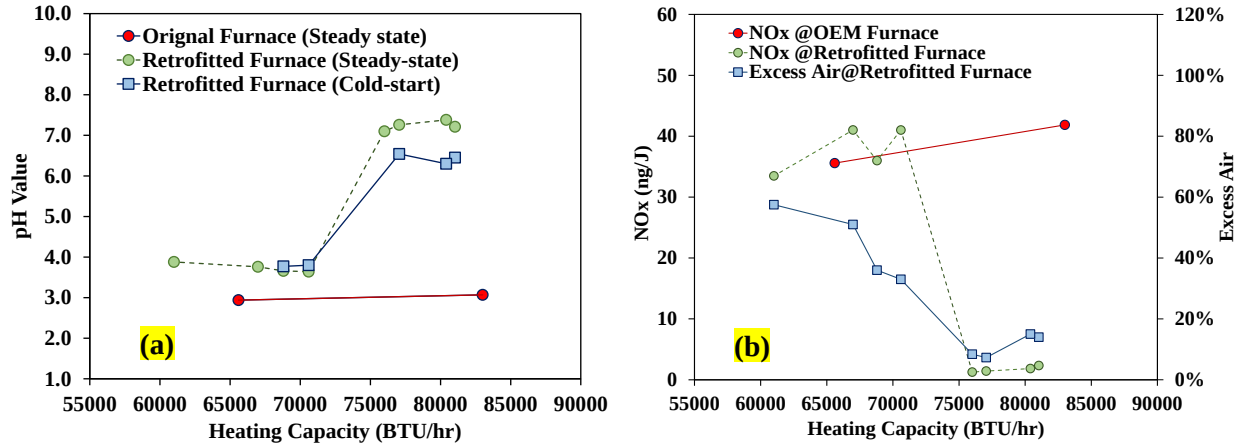

Figure 12: (a) Condensate acidity and (b) NOx emissions comparison of the AGR-enabled condensing furnace with the original OEM furnace, as a function of the furnace heating capacity.

Figure 13(a) displays the comparison of AFUE between the original OEM condensing furnace and the AGR-enabled condensing furnace. The retrofitted unit achieves slightly better AFUE. The major reason is that the AGR installed in the retrofitted furnace is able to oxidize CO, HC, methane and formic acid. As a result, the furnace recovers energy from the unburnt fuel energy which typically is lost in the original OEM furnaces. This observation is confirmed by Figure 13(b), which shows the AGR inlet and outlet temperatures. These clearly indicate that the temperature is significantly increased at the exit of the AGR. Therefore, the monolithic AGR component enables the furnace to efficiently achieve not only SOx trapping

and NOx redox to N_2, but also performs formic gas/CO/HC/CH_4 oxidation. Therefore, the AGR component can be utilized in a condensing natural gas furnace design to alleviate corrosion and long-term environmental issues associated with acidic condensates and flue gas emissions as well as enabling more efficient furnace operation. Existing commercial condensing furnaces employ air entrainment to control combustion temperature, energy efficiency and NOx emissions. With the air entrainment technology, however, it is hard to achieve SOx trapping and ultralow NOx emissions, and expensive stainless-steel alloys are required to avoid serious corrosion issues.

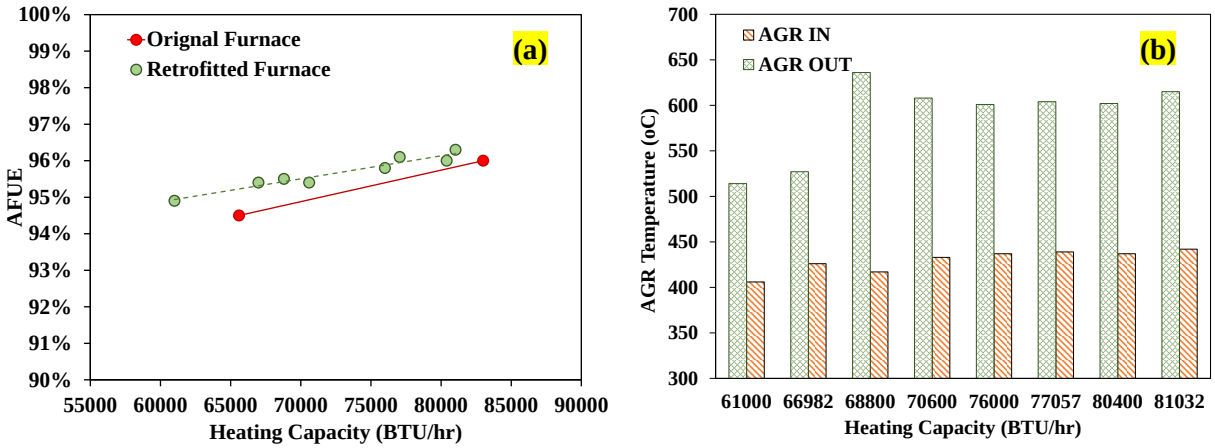

Figure 13: Performance comparison between the retrofitted condensing furnace with the AGR and the original OEM condensing furnace at various heating capacities. (a) AFUE; (b) AGR inlet and outlet temperatures.

4.2 AGR Regeneration Impact on the Performance

Figure 14 shows an example of SOx release during regeneration activities after carrying out the 800-minute trapping experiment at 100 ppm SO_2 exposure and 250°C. The full-scale SOx trap experiment was carried out in an offline regen reactor (see Figure 14). The data shown in a yellow color were collected during trapping of 100 ppm SO_2 in synthetic furnace exhaust, and the data shown in a red color were collected during the regeneration phase. The observation shows minimal SO_2 breakthrough during the trapping phase (i. e. < 3ppm), but an enormous amount of SO_2 stored on the catalyst came off rapidly during regeneration. The results show that the SO_2 concentration during regen hits over 10000 ppm. This indicates that offline regeneration of a full size AGR is achieved at moderate temperatures. In the 800-minute trapping experiment, the amount of the trapped SOx is 0.35mole, which is equivalent to trapping furnace SOx emissions from the representative cities in US heating regions I-V for not less than 3 years. The average residential natural gas furnace in U.S. climate heating regions I-V is estimated to generate 0.07 ~ 0.1 mole SOx annually [43]. Furthermore, the amount of 0.35mole is not far from the threshold limit of the SOx storage capacity in the AGR. The authors estimated that the SOx storage capacity in AGR could cover at least 3 years of furnace SOx emissions. This means that regeneration events may be required every three years. Once the AGR degrades, the AGR component can be disassembled from the new furnace to carry out its regeneration and recycle the trapped SOx in an offline regen reactor. This also avoids environmental issues related to SOx slip.

To understand the impact of AGR regeneration activities on the AFUE, pH values, and emissions from the retrofitted furnace, a full-size AGR, which experienced the off-line AGR component regen events, was installed into the retrofitted furnace. The tested AGR experienced three off-line AGR component regen events after each trapping experiment at 100ppm SO_2 exposure and 250°C. The accumulated SOx storage

capacity in the AGR would be equivalent to 10 years of furnace SOx emissions. The results are shown in Figures 15(a)-15(c). ANSI/ASHRAE standard testing procedures were carried out at various heating capacity rates. Overall, the performance trend is similar to the fresh AGR tests that were conducted without experiencing regen events. The deviations are within the measurement resolution errors. The AGR subjected to regeneration activities functioned well – achieving both neutral condensate and ultra-low NOx emissions. Furthermore, the AGR that was subjected to regeneration activities achieved a slightly higher AFUE.

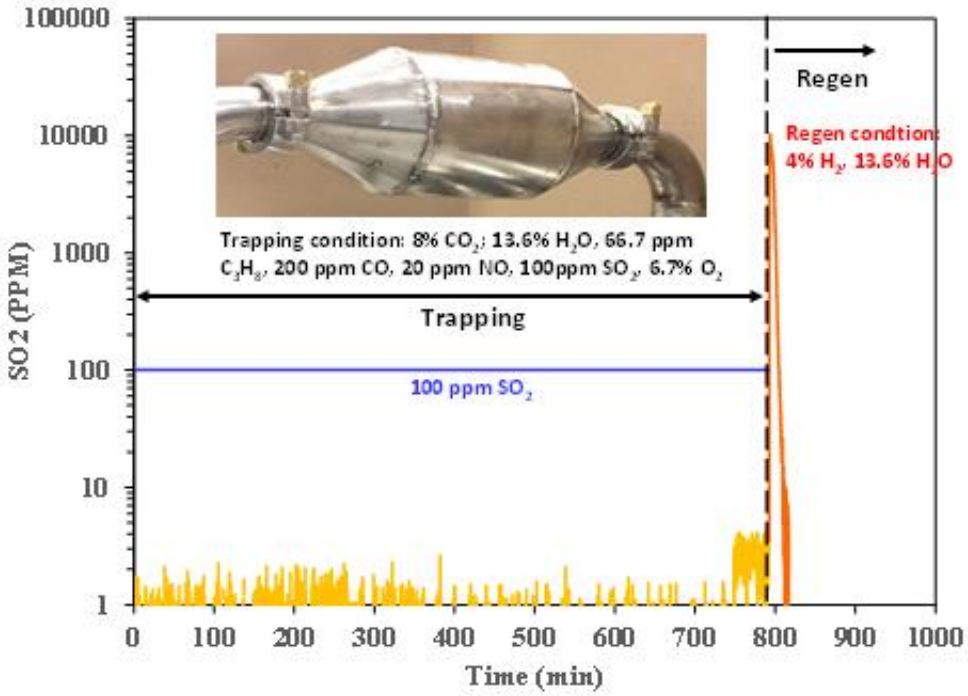

Figure 14: Off-line regeneration of a full-size 2-liter AGR component after carrying out the trapping experiment at 100ppm SO_2 exposure and 250°C.

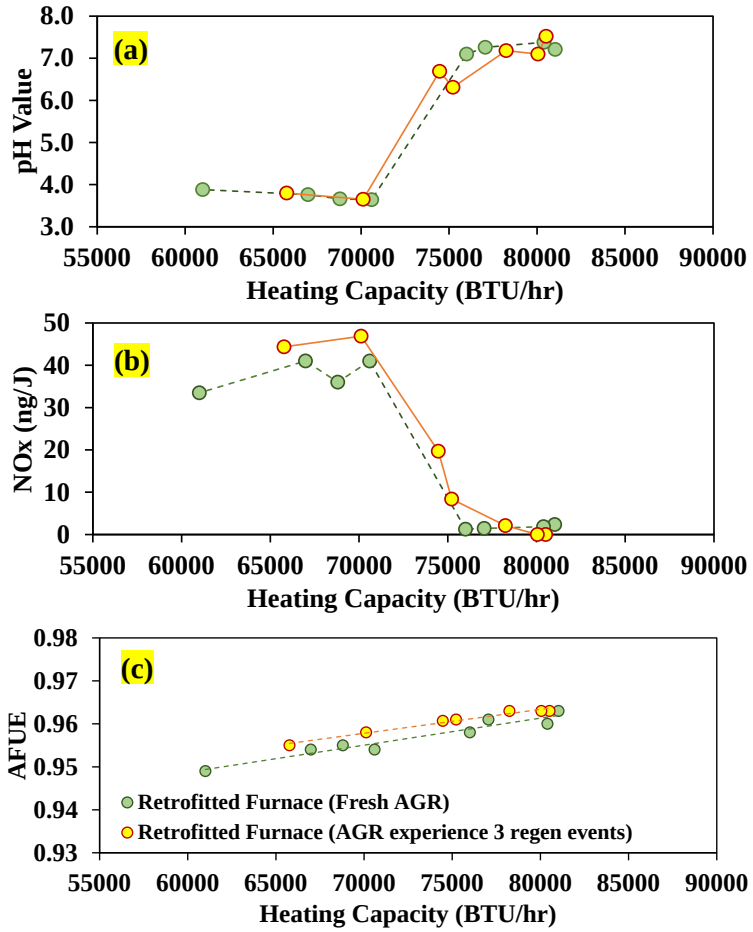

Figure 15: The comparison of (a) condensate acidity, (b) NOx emissions and (c) AFUE between the fresh AGR and the AGR experienced 3 regen events in the retrofitted furnace as a function of various steady-state heating capacities.

4.3 400-Hour Reliability and Durability Test

The condensing furnace with the AGR component was in operation at 23.4 kW (80,000 BTU/h) for approximately 400 hours to understand the reliability and durability of the retrofitted unit and AGR component. During the test, a sample of condensate was collected, and its pH value was recorded daily. Figure 16 shows that the pH values of the condensate collected during the tested period. In general, the retrofitted furnace performed well. Some minor spikes in pH were observed over the testing period, but the deviations are still within a reasonable range. The recorded pH values remain around 7 during the tests, indicating 99.99% of acidic gas removal. The collected condensate remained colorless and did not include any deposits, which indicates there was no physical damage in the AGR catalyst component. All the furnace components, including fan and control, continued to operate normally.

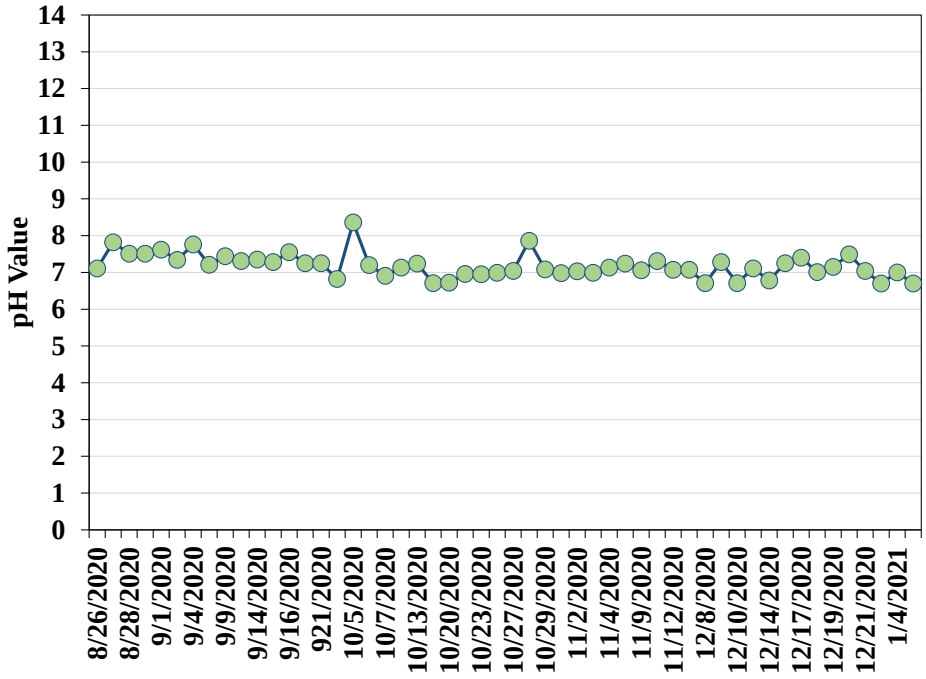

Figure 16: The pH value of steady-state condensate samples collected from the retrofitted condensing furnace with the AGR component during a 400-hours of reliability and durability test.

Figure 17 shows the retrofitted condensing furnace performance before and after the 400-hour reliability and durability test. The unit's pH values, NOx emissions, and AFUE were tested at various heating capacities and compared the performance of the original OEM furnace as a baseline. Figure 17(a) shows that the pH of the collected condensate in all cases after the 400-hour reliability and durability test achieved a pH above 5 while the pH of the collected condensate at the heating capacity of >67 kBTU/h cases is close to 7. In contrast, the data measured from the fresh retrofitted furnace before the 400 hour testing shows that the pH of the collected condensate at <75 kBTU/h cases is below 4. Figure 17(b) compares NOx reduction between the fresh and 400-hour AGRs. During the 400-hour test, the AGR still enabled 0-3 ng/J of NOx emissions from the retrofitted furnace. For comparison, the NOx emissions from the fresh OEM furnace without the AGR were 35-40 ng/J while emissions from the retrofitted furnace with fresh AGR were 1.0-2.3 ng/J of NOx. Thus, both fresh and 400-hour AGR components reduce more than 90% of NOx emissions in the retrofitted furnace. These values are well under the 14 ng/J required by the new California standards. Figure 17(c) shows that long-term operation does slightly degrade the AFUE performance of the AGR-enabled furnace, although it remains close to the original furnace performance.

In addition, the authors observed that, compared to the fresh AGR-enabled furnace, the low NOx zone extended to low heating capacities in the 400-hour AGR-enabled furnace. The major reason is that after the 400-hour reliability and durability test, the furnace seems to shift its operation to less lean combustion conditions (see Figure 17(d)). The AGR component clearly works better for NOx reduction close to or at stoichiometric conditions. This indicates that there exists substantial space to optimize condensing furnaces in achieving stoichiometric combustion. Consequently, condensing furnaces enabled with AGR component have potential to be designed into more compact and less expensive units.

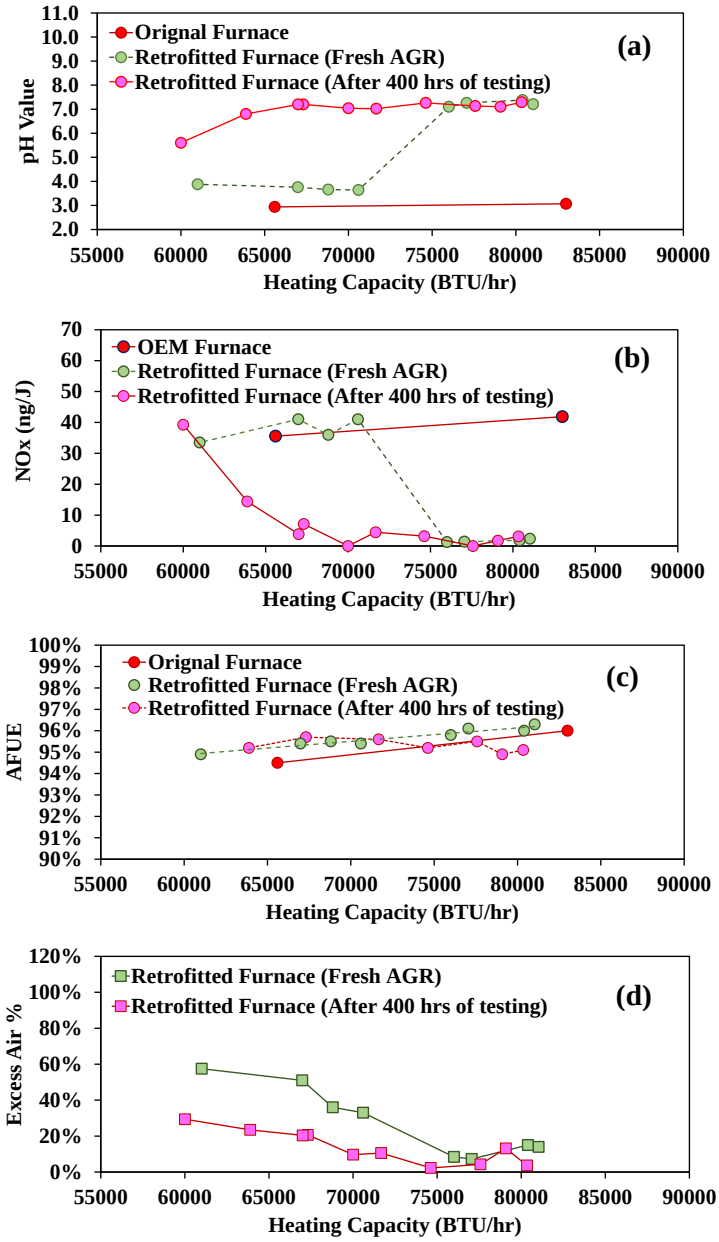

Figure 17: Comparison of (a) pH values, (b) NO_x emissions, (c) AFUE, and (d) combustion condition of the OEM furnace, the retrofitted condensing furnace with a fresh AGR, and the retrofitted furnace after 400 hours of testing at various heating capacities.

5. NONDESTRUCTIVE NEUTRON IMAGE DIAGNOSIS OF AGR

5.1 NCT and 3D Volume Visualization

Neutron imaging was performed at the CG-1D neutron imaging beamline at ORNL's High Flux Isotope Reactor. Figure 18(a) shows the schematic of the CG-1D beamline. Figure 18(b) shows the AGR samples mounted on the rotation stage of sample table. Cold neutrons with wavelengths ranging from 0.8 to ~6 Å were used for imaging in the study. A 100 μm 6LiF/ZnS scintillator was used to convert the transmitted neutrons into light signal, which was then recorded by a charge-coupled-device (CCD) with effective pixel size of 42μm by 42μm to generate the grayscale 2D projection as raw data [44]. The resulting neutron transmission is described by the Beer-Lambert law [45, 46]: $I = I_0 e^{-\sum \mu_i x_i}$, where I0 is the incident intensity, I is the transmitted intensity, μi is the attenuation coefficient of element i, and xi is the effective thickness of element i along the incident beam path. The attenuation coefficient μi is given by $\mu_i = \sigma_i \rho_i N_A / M_i$, where σi is the total neutron cross-section (including absorption and scattering) of element i, ρi is the density of element i, NA is the Avogadro's number and Mi is the molar mass of element i.

To achieve a high-quality computed tomography measurement, the 2-liter sample was mounted on a large rotation stage, which was rotated through a 360° range with a step size of 0.17°. At each angle, an image with a 30 s exposure time was recorded as a projection. After collecting over 2,000 projections, the neutron attenuation image of the AGR volume was successfully reconstructed by filtered-back-projection using MuhRec [47]. A 3D visualization was generated, and data analysis was performed using Amira [48], which is developed by Thermo-Fisher Scientific in collaboration with the Zuse Institute Berlin.

Unlike other methods, such as X-ray or electron imaging, which are typically attenuated significantly by metals, neutrons can penetrate many metals (i.e., steel in this case) with much less absorption. This enables the use of neutron imaging to probe structures inside metallic assemblies such as the AGR catalyst. As neutrons interact with the nucleus of an atom, the absorption and scattering of different elements varies greatly. Compared with metallic elements, the scattering and absorption of neutrons by lighter elements (e.g., H) are much more prominent in NCT. Soot particles typically result from condensation of vaporized organic matter, usually through a number of polycyclic aromatic hydrocarbons, and the chain of aromatic rings then grows through a fast polymerization process (i.e., replacement of H atoms by C_2H_2 groups). Therefore, a substantial amount of hydrogen atoms should be present in the soot particles, and the neutron contrast can be exploited to image the accumulated soot particle layer owing to the deposition of hydrocarbon. In particular, neutron imaging is well suited to nondestructively survey the AGR component within a metal shell. In the study, the spatial mapping utilized neutron imaging to spatially detect the structure drawback and/or damage of the aged AGR component and survey the soot load distribution and density variation within the aged AGR component. To the authors' knowledge, this is the first time that NCT has been used to nondestructively provide spatially resolved 2D and 3D representations of the aged AGR component.

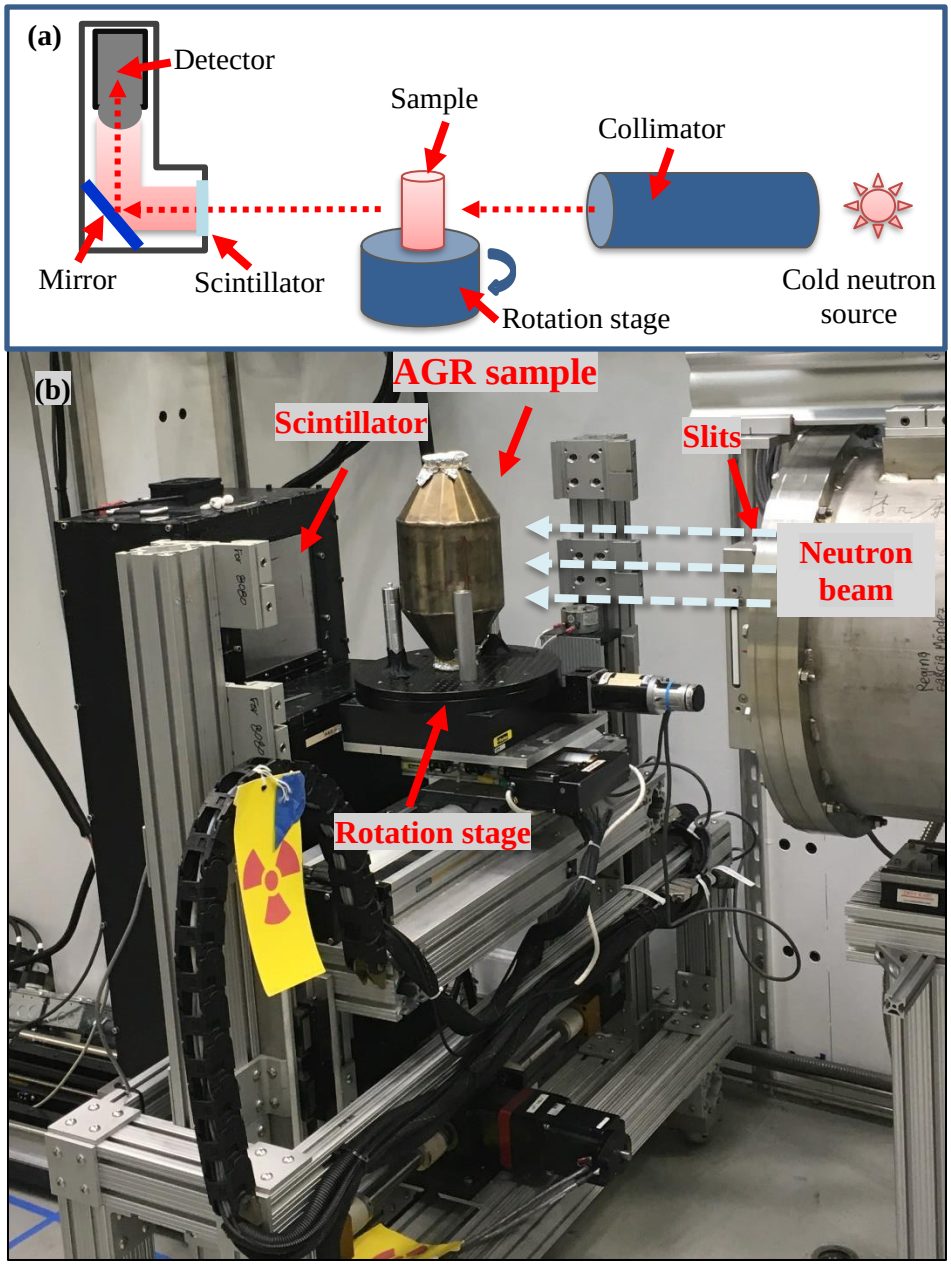

Figure 18: (a) Schematic of the instrument configuration on the CG-1D beamline. (b) Full-size aged AGR component placed on the rotation stage of the sample table in the neutron imaging beamline.

5.2 Aged AGR and Soot particles

The aged AGR was disassembled from the furnace unit. Figure 19(a) shows that the soot particles accumulated on the metal net mounted in the AGR's inlet cone zone, and the AGR's outlet cone zone appears to have much less soot. Figure 19(b) shows the sample soot particles collected from the AGR. These soot particles include the deposition of unburnt HC and carbon [49, 50]. The collected particle samples were analyzed using SEM at ORNL. Figure 19(c) shows SEM images of the soot particles. It is evident that the soot particles produced are fractal aggregates composed of agglomerated small spheres, which are the deposition of unburnt HC and carbon. The morphology of soot particles in this study (i.e., the

size, number, and arrangement of the primary spherules) is similar to that of particles produced by diesel engine combustion [50]. Figure 20 shows the Raman spectra of the soot particles before and after oxidation in air at 900°C. Owing to the presence of strong fluorescence in visible Raman measurements, only UV Raman (excitation at 244 nm) was able to detect a broad band at around 1615 cm^{-1} with a weak band at ~1385 $cm^{-}$for the freshly collected sample, which indicates the presence of hydrogenated amorphous carbon in the soot particles [51]. Oxidation in air at 900°C can completely burn away the amorphous carbon, as indicated by the absence of the Raman band at ~1615 cm^{-1} in the sample surveyed.

The deposited amorphous carbon is likely caused by the incomplete combustion of the natural gas furnace owing to inappropriate condensate drainage. In the reliability and durability test, the condensate drainage pipe of the prototype furnace was connected to a water tank to collect condensate. When the pipe exit was flooded with the collected condensate, it slowed the condensate drainage, increased the backpressure of the flue gas, and even accumulated the condensate in the condensing heat exchanger and blocked flue gas flow. Figure 21 shows the furnace functioning appropriately at the beginning of the testing day, and then the unit control system automatically turns off and on when the drainage pipe exit is submerged 3 hours later. As more condensate accumulates in the furnace, the on/off control activities become more frequent. Frequent on/off control activities result in severe combustion failures in the furnace, which lead to amorphous carbon deposits in the AGR. This indicates that proper condensate drainage is critical for an AGR-enabled furnace.

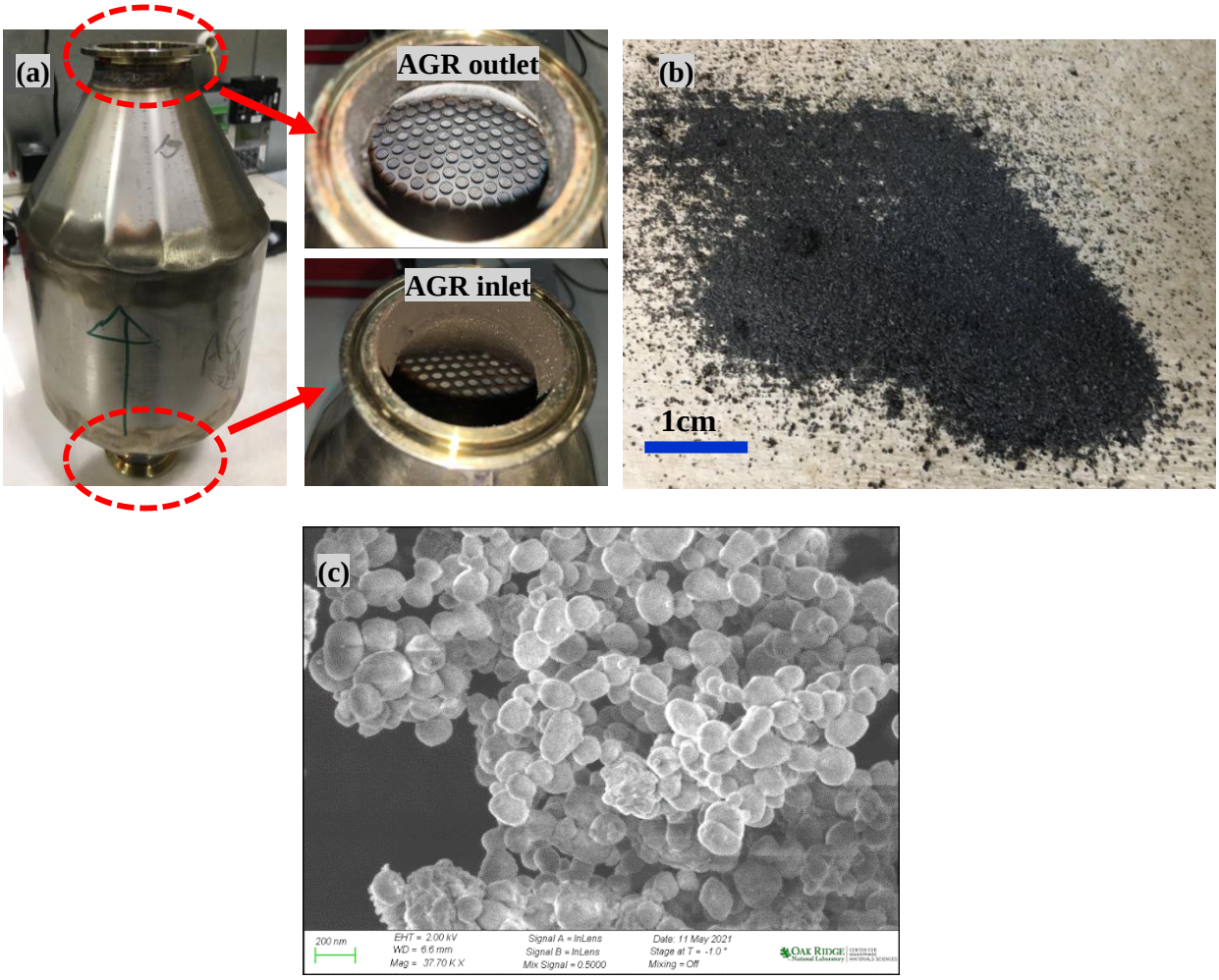

Figure 19: (a) Disassembled aged AGR from the tested furnace and its inlet and outlet view. (b) Soot particle found from the AGR. (c) Example of SEM images of soot particles collected from a 400-hour reliability and durability test.

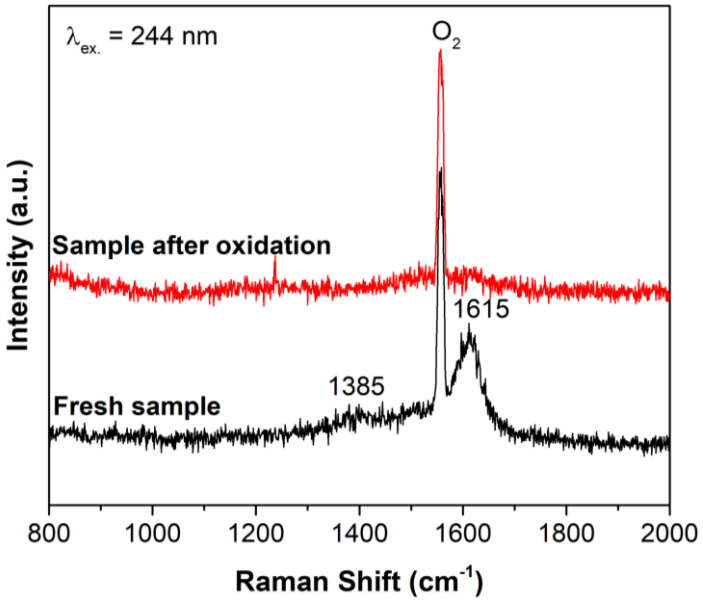

Figure 20: Diagnosing amorphous carbon in the sample using the Raman spectroscopy method. Laser excitation at 244 nm; the sharp peak at 1555 cm^{-1} is caused by the stretching mode of O_2 from air during the measurement at ambient conditions.

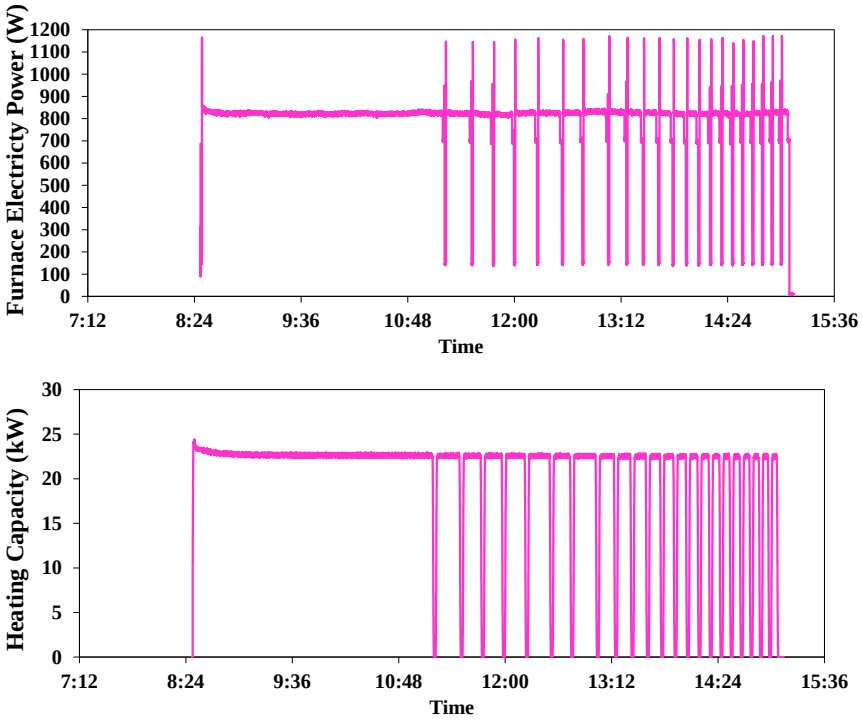

Figure 21: Malfunction of the AGR-enabled furnace related to inappropriate condensate drainage. The data was collected on September 9, 2020.

5.3 Nondestructive Diagnosis of AGR using NCT

Figure 22 shows the neutron spatial mapping of the aged AGR component with a 3D depiction of the component and slice views of representative cross sections. In the figure, the neutron attenuation coefficient reflects how strong a sample attenuates neutrons by scattering and absorption. In this work, soot particles that contain light elements such as hydrogen would significantly contribute to the attenuation coefficient, whereas the attenuation caused by catalyst blocks and the metal shell is negligible. Therefore, the higher attenuation coefficient indicates denser hydrogen content and higher soot particle loading in the catalyst sample. In the 3D computed tomography (see Figure 22(a)), the reconstructed 3D volumetric data provides structural analysis of the inside of the AGR sample. A comprehensive 3D neutron spatial mapping animation of the aged AGR component is also generated. A few cross-section view (see Figure 22(b)) are selected at different locations within the 3D structure for data analysis and detailed diagnosis.

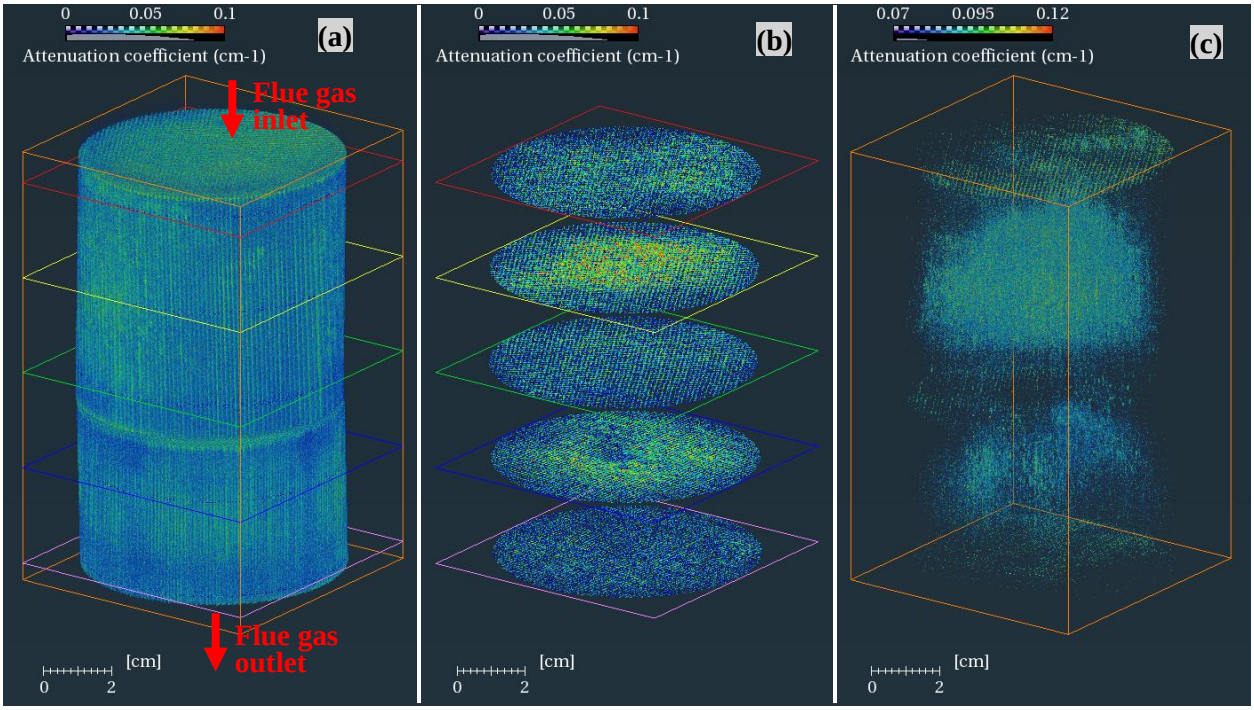

Figure 22 Neutron spatial mapping of the aged AGR component with the direction of flow from the top (inlet) to the bottom (outlet). (a) A 3D depiction of the whole component. (b) Slice views at representative cross sections marked by square outlines. (c) the scaled 3D neutron spatial mapping with the attenuation coefficient of 0.07~0.12.

As shown in Figure 22(a), the aged AGR catalyst consists of two honeycomb-like monoliths with identical material formulation. The discontinuity of the assembly is captured by the tomography (Figure 22(a)) and is shown at about one-third of the way from the bottom. The AGR component was subjected to flue gas, which entered the top block and then went through the downstream block. The tomography data confirms the integrity of the assembly and shows no deformation or broken channels within the imaged area of AGR component. This indicates that the developed AGR catalyst and substrate remain reliable and durable after the 400-hour operation. However, flow in some channels was substantially restricted during the 400-hour durability test due to soot particle accumulation along the channels.

Figure 22(b) shows the cross-sectional views at different locations marked with the corresponding square outlines on Figure 8a to indicate the entrance (red square outline), middle (yellow square outline), and exit (green square outline) regions for the top block and the middle (blue square outline) and exit (purple square outline) regions for the bottom block. Neutron attenuation is higher in the top block than in the downstream block. This shows the top block had more significant soot accumulations than the downstream block as flue gas flowed from the inlet to the outlet. Moreover, the results revealed substantial soot accumulations in the middle region of the top block. Significant soot accumulation was also found in the central regions along the cylindrical cross sections in both the top and bottom blocks, as shown in Figure 22(b). Figure 22(c) shows the scaled neutron spatial mapping with the attenuation coefficient of 0.07~0.12 in order to highlight the internal heavy soot accumulation. The spatially soot distribution further confirms the results of soot volumetric coverage derived from Figures 22(a) and 22(b).

To examine the component more closely, we also analyzed a subset of the volume (e.g., in the center of the component (see Figures 23(a) and 23(b)). The distribution of the particle accumulation in the middle of the top block is visibly higher than at the entrance and exit of the top block. Again, the bottom block also shows significantly higher density in the middle compared to the entrance and exit regions. The average profile of volumetric coverage of soot particles in the extracted volume of the catalyst sample is evaluated using a conversion of the measured attenuation coefficients to the particle volumetric coverage based on the estimated compositions of the soot in the extracted volume, as seen in Figure 23(c), which shows the strong variation from the top entrance to the bottom exit. In the top block, from a distance of 2.5–5.5 cm away from the inlet, the distribution of the accumulated particles reached a plateau, which is consistent with the situation of a laminar flow in the AGR channels that can distribute the soot along the channel walls. This region had the highest particle accumulation in the AGR component because the solid turbulent flow that occurred before and after the blocks had less impact on the middle section. As a result, fewer particles accumulated in the entrance and exit regions than in the middle region. Compared with the top block, the bottom block (~8–13 cm) has much lower soot accumulation, and the soot gradually decreases toward the exit. The methodology of determining soot particle volumetric coverage in the aged AGR sample is based on comparison between the fresh and aged AGR catalysts.

In Figure 23, the significant spikes at the edge of the two blocks (e.g., near 0, 8, and 13 cm) indicate an abnormally high hydrogen concentration, which may be caused by higher moisture adsorption owing to its close proximality to the ambient environment after the tests. Another possibility is that the turbulent flow from the edge causes higher accumulation of soot particles. Further study with a fresh sample carefully sealed after the aging test could help determine the exact cause.

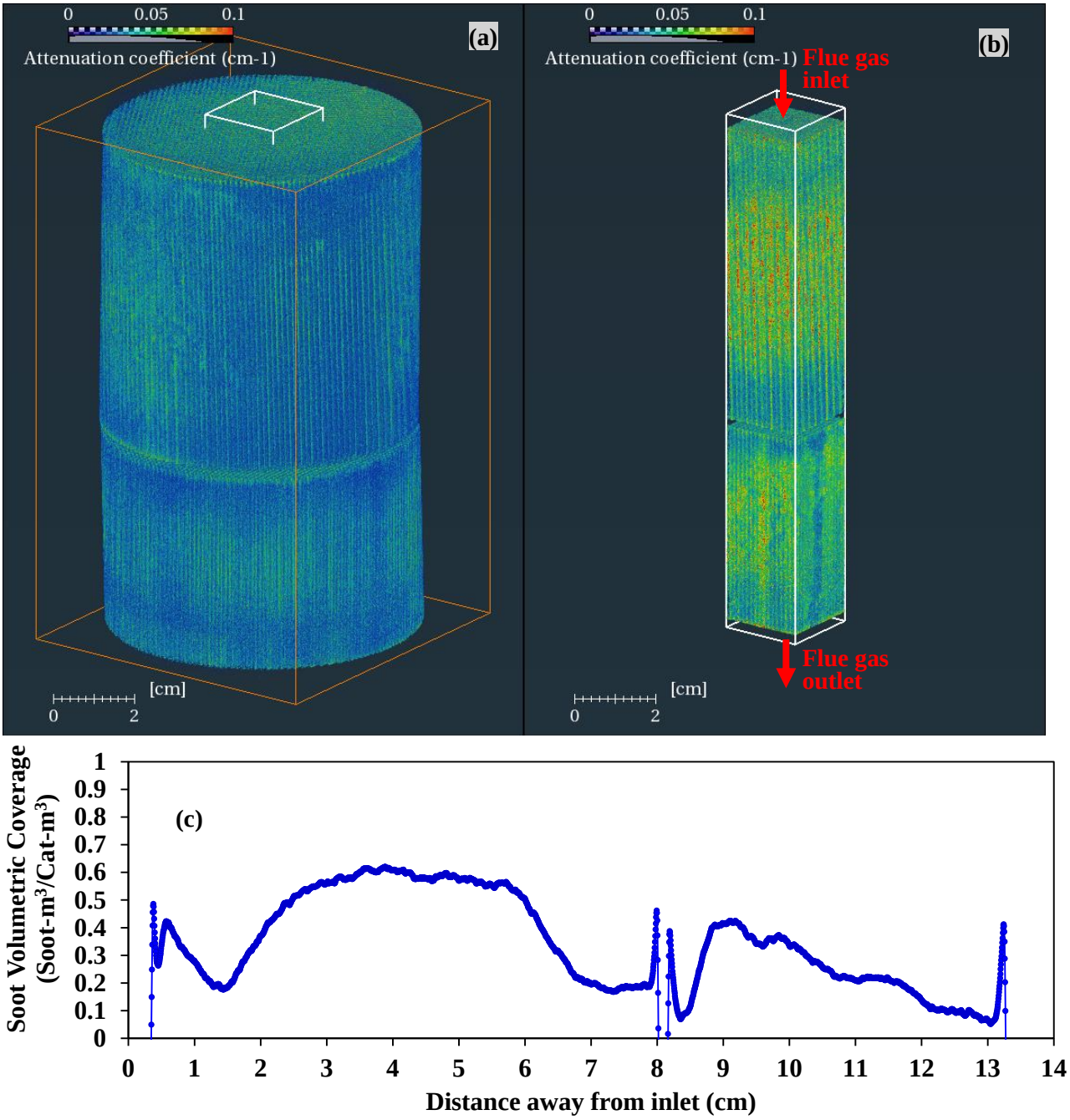

Figure 23: Neutron spatial mapping of the aged AGR component with the direction of flow from the top (inlet) to the bottom (outlet). (a) A 3D depiction of the whole component; (b) slice views at given cross sections as marked by the square outlines; (c) the average profile of soot particle volumetric coverage in the catalyst sample based on the extracted volume of Figure 23(b).

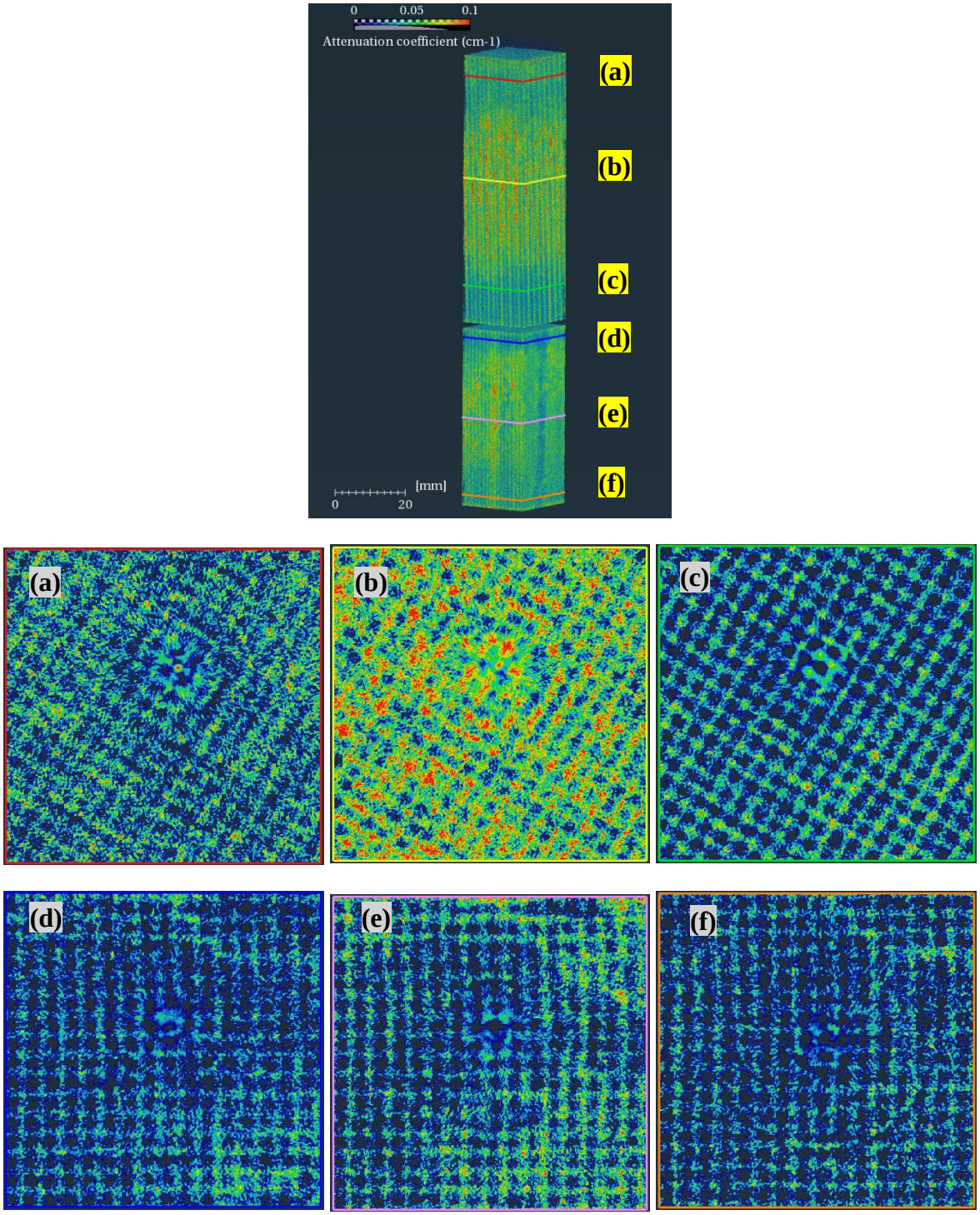

Figure 24: Detailed spatial resolution of the structural and particulate distribution of individual AGR channels captured using neutron imaging. Each channel is around 1 mm by 1 mm. The views at given cross sections are marked by the square lines at (a) 1.0 cm, (b) 4.0 cm, (c) 6.5 cm, (d) 8.5 cm, (e) 10.5 cm, and (f) 13.0 cm.

As an example, Figure 24 shows the more detailed spatial resolution of the structural and particulate distribution of individual AGR channels at different locations revealed in NCT. The dark blue in the figure represents empty space inside the AGR. The results clearly confirm that the deposited particles accumulated heavily in some channels in the middle of the top block, and the flow of some channels were substantially restricted. The square shape of the channels is still evident. Although some channels in the middle region of the top block had heavy particle deposits, the channels at the entrance and exit regions of the top block have significantly less particle deposits. Significantly fewer particle deposits were found in the downstream block compared with the middle region of the top block.

Overall, the spatial detail of this uneven distribution throughout the AGR component, particularly for the phenomenon of the heavy aggregates in the middle of the top block and in the central region along the cross section, are revealed by the NCT. The large amount of volumetric data from the NCT provides very rich structural information for the AGR sample, and the detailed internal views and analysis can answer specific questions about the catalyst sample. In particular, the rich structural information will help with redesigning and co-optimizing the accessory parts (e.g., connection cones) and the monolithic channel size/shape of the AGR component; modifications to these components could enable a uniform and self-cleaning flow pattern to enter all monolithic channels of the AGR component. If a new AGR design can mitigate significant soot aggregation in the middle of the top block and in the central region along the cross section, then AGR-enabled furnaces could perform appropriately even during adverse events, which is vital to the commercialization of AGR and AGR-enabled furnaces. The unique and detailed information obtained from the reconstructed tomographic data of the AGR with a metal shell cannot be obtained non-destructively by other means.

6. EXPLORATION OF NEW AGR WITH LOW PRECIOUS METAL LOADING

6.1 New AGR with Low Precious Metal Loading

A new AGR catalyst with low precious metal loading was explored to identify a pathway of optimizing AGR material loading and maximizing acidic gas reduction at low cost. The new AGR catalyst was fabricated to include two catalyst blocks, as shown in Figure 25. Table 4 lists the key material formulation for each catalyst block. The first block formulation is capable of trapping SOx, NOx redox to N_2, and oxidation of CO/HC/CH_4/formic gas oxidation. The catalyst block adopts the same catalyst material formulation as listed in Table 1. The key chemical reaction mechanism is described in elsewhere [52, 53]. The second block formulation was designed with Ce-based oxygen-storage material and low Pt/Rh loading to enhance NOx redox to N_2 and oxidation of CO/HC/CH_4/formic gas, particularly under slightly lean or stoichiometric conditions. Compared with the first-generation AGR catalyst sample using only the block with material formula I, the new AGT monolith sample reduced precious metal loading by 38%.

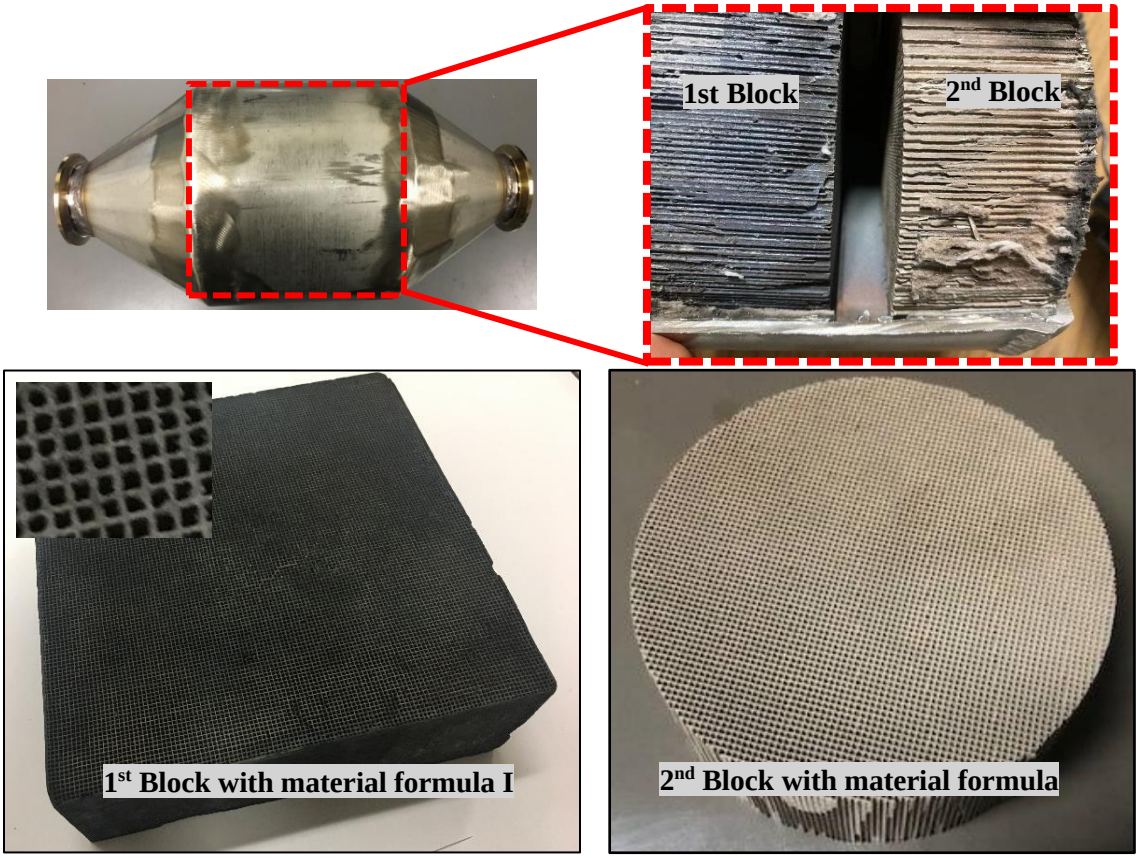

Figure 25: The second AGR catalyst sample with two catalyst material formulae.

Table 4: The material composition used in the new AGR catalyst sample

Material recipe		Block with material formula I	Block with material formula II
Materials and composition	TiO_2 loading	195 g/L (Anatase TiO_2)	-
	Cu loading	24.4 g/L	-
	Pt/Rh loading	4.27 g/L (Pt only)	0.53 g/L (Pt/Rh)
	CeO_2 loading	-	90-120 g/L
	Other loading	-	IP material (cannot show)
TiO_2 surface area		50 m^2/g	-
CeO_2 surface area		-	150 m^2/g

6.2 Effect of AGR Components on Furnace Performance

The retrofitted condensing gas furnace integrated with the new AGR component was tested for AFUE, condensate pH values, and emissions at various heating capacity rates. Figure 26 shows that the new AGR component with low precious metal loading successfully achieves neutral condensate and ultralow NOx emissions. Figure 26(a) compares the condensate acidity of the retrofitted AGR-enabled furnaces with the original OEM furnace. Compared with the first-generation AGR catalyst with higher precious metal loading, the new AGR catalyst with low precious metal loading achieves the similar performance of the neutral condensate. The effect of the new AGR component on NOx reduction is shown in Figure 26(b). Compared with 35-40 ng/J of NOx emissions from the original OEM furnace, the AGR with heavy Pt loading enables the retrofitted furnaces to achieve 1-2 ng/J of NOx emissions, and the AGR compoent with low Pt/Ph loading enables the retrofitted furnaces to achieve ~0 ng/J of NOx. The low precious metal loading of the new AGR catalyst does not impair the AGR performance in achieving ultralow NOx emissions, and achieves even slightly better NOx reduction. However, to achieve the neutral condensate and ultralow NOx emissions, the furnaces must be operated within a narrow excess air or a narrow air-to-fuel ratio near stoichiometric conditions to ensure high conversions, as shown in Figure 26(c).

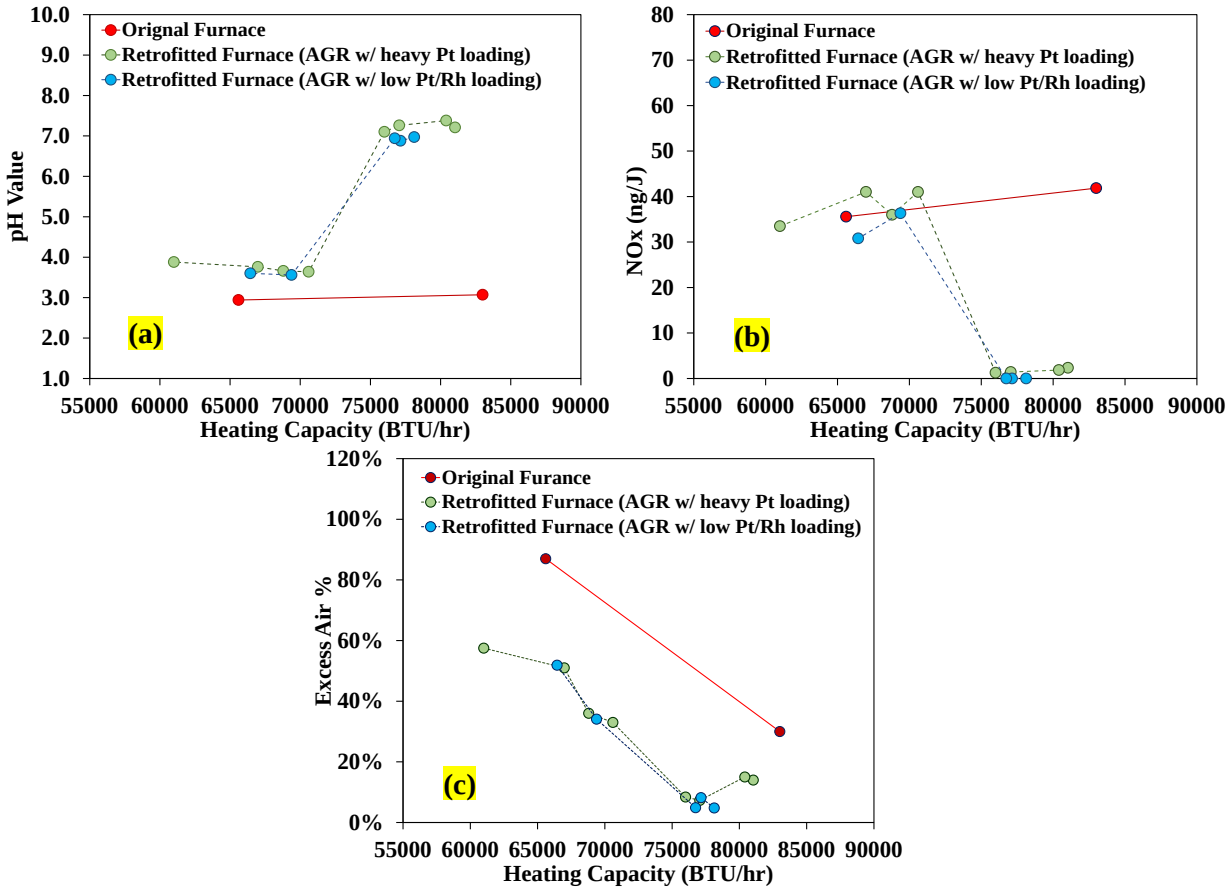

Figure 26: (a) Condensate acidity, (b) NOx emissions, and (c) combustion excess air of the AGR-enabled condensing furnaces compared with the original OEM furnace, as a function of the furnace heating capacity. Here 1 kW is equal to 3.41 kBTU/hr.

Figure 27 compares the AFUE of the original condensing furnace and the retrofitted condensing furnaces with different AGR components. Compared to the first-generation AGR component with higher Pt loading, the new AGR component with low Pt/Rh loading further improved the AFUE by 1-2%. The furnace with the AGR component with low Pt/Rh loading achieved a maximum AFUE of 97%, which is meaningfully higher than the original furnace. The major reason for this efficiency is that the new AGR component installed in the retrofitted furnace can efficiently oxidize CO, HC, CH_4, and formic acid. Therefore, the furnace recovers energy from the unburnt fuel energy which is typically lost in the traditional OEM furnaces. Figure 28 shows a cold-start CO oxidation comparison between the retrofitted condensing furnace with the low Pt/Rh loading AGR catalyst and the traditional OEM condensing furnace. Clearly, the AGR component enables the furnace zero CO emissions at the cold start compared with up to 400PPM in the OEM condensing furnace.

Overall, the new AGR component enables the furnace to efficiently achieve not only SOx trapping and NOx redox to N_2, but also formic gas/CO/HC/CH_4 oxidation. Therefore, the AGR component can be utilized in a condensing natural gas furnace design to alleviate corrosion and long-term environmental issues associated with acidic condensates and flue gas emissions, as to enable more efficient furnace operation. The new AGR component with low Pt/Rh loading results in improved AFUE without impairing the performance in achieving a neutral condensate and ultralow NOx emissions.

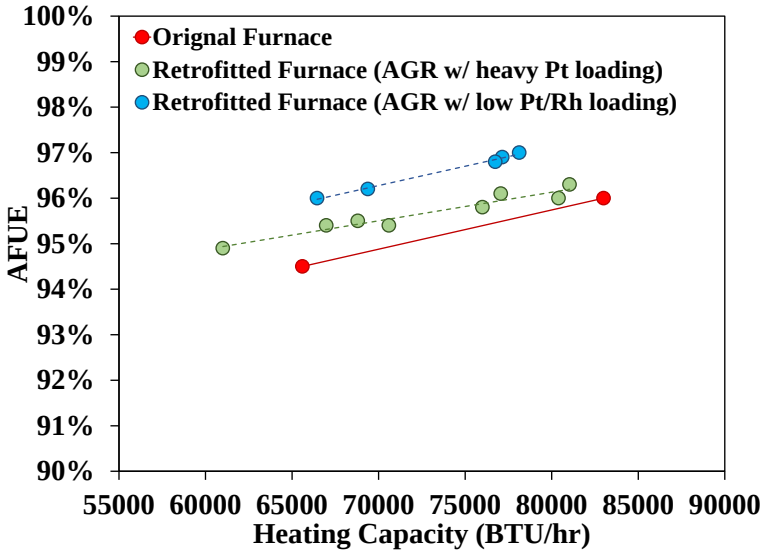

Figure 27: Performance comparison between the retrofitted condensing furnace with the AGR and the original OEM condensing furnace at various heating capacities. (a) AFUE; (b) AGR inlet and outlet temperatures. Here 1 kW is equal to 3.41 kBTU/hr.

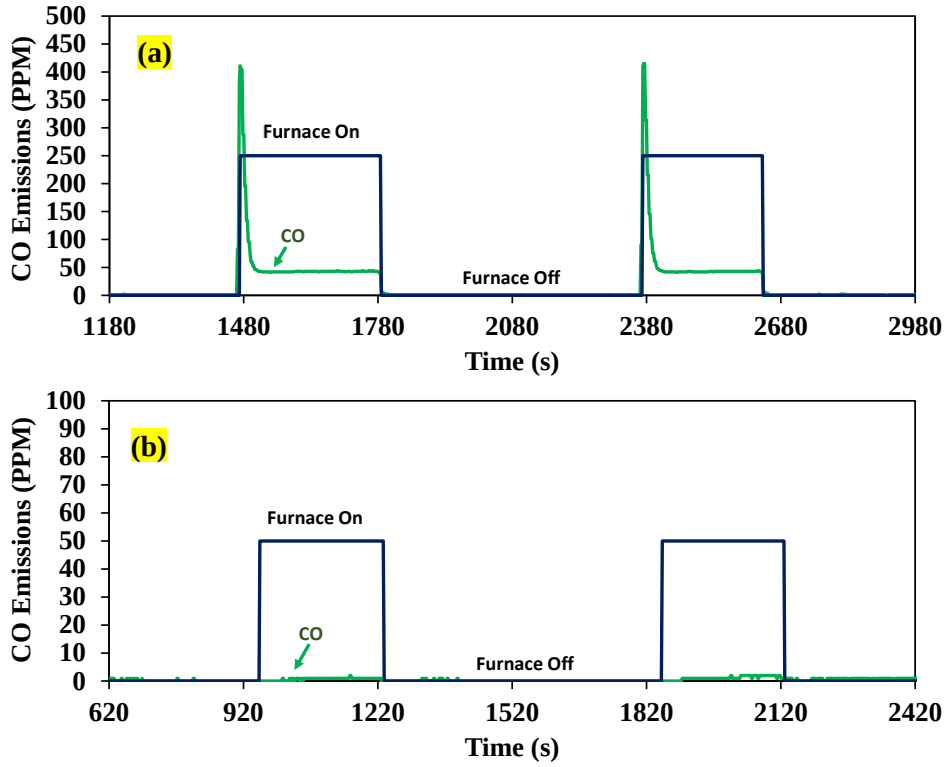

Figure 28: Cold-start CO oxidation comparison between the retrofitted condensing furnace with the low Pt/Rh loading AGR and the original OEM condensing furnace at a heating capacity of 78 KBTU. (a) the original OEM condensing furnace AFUE; (b) the retrofitted condensing furnace with the AGR with low Pt/Rh loading.

7. CONCLUSION

An ultra-clean and efficient natural gas furnace was demonstrated by employing an AGR component that can remove more than 99.9% of the acidic gas products of combustion. The AGR catalyst was fabricated with a monolithic substrate washcoated with low-cost TiO_2 and CuO_2 and includes the precious metal Pt. The AGR catalyst is capable of continuous NOx redox, oxidation of CO/HC/CH_4 and formic gas, and trapping of SOx. In the experimental testing of a full residential furnace, the AGR technology offered the following benefits: (1) a neutral furnace condensate with a pH of ~7, allowing its safe release into the sewer system thus eliminating a second drainage system; (2) trapping and removing nearly all SOx emissions; (3) NOx emissions at nearly 1-2 ng/J, more than 95% lower than new emissions standards in California; (4) the use of a low-cost heat exchanger as a condensing HX since the condensate is not acidic, avoiding the need for expensive stainless steel alloys; and (5) unburnt fuel energy recovery to boost efficiency. The AGR technology provides a potential transformative path for weatherized or non-weatherized natural gas condensing furnaces in meeting restrictive emission regulations and reducing environmental impacts of furnaces associated with soil, water and air. Moreover, it can help reduce furnace equipment cost, as well as installation and maintenance costs, leading to greater market penetration of high-efficiency condensing furnaces.

The AGR component and AGR-enabled furnace performance were broadly tested to determine their effects on long-term reliability and durability, as well as SOx storage and regeneration activity. The results show that the AGR component is appropriately integrated with natural gas furnaces, and the acidic gases of SOx, NOx and formic gas/CO/HC will be continuously adsorbed, redoxed, and oxidized, respectively, from the flue gas during a regular heating season, except for occasional regeneration activities for SOx trapping. The AGR regeneration does not impair the performance in achieving a neutral condensate and ultra-low NOx emissions, and the AGR catalyst subjected to regeneration activities continued to function well and achieved slightly better AFUE compared with the original OEM furnace. The 400-hour reliability and durability test of the retrofitted condensing furnace with the AGR component showed that the furnace unit achieved a neutral furnace condensate with a pH of ~7 and enabled 0-3 ng/J of NOx emissions, but the 400-hour operation slightly degraded the AFUE. After this testing, the furnace operation changed because of amorphous carbon deposits and incomplete combustion caused by inadequate condensate drainage in the test. Thus, proper condensate drainage is critical for AGR-enabled furnaces. All the furnace components, including fan and control continued to operate normally during reliability testing. This indicates high reliability and durability of the AGR technology, as well as its highly compatibility with commercial furnaces in the market.

NCT was employed to survey the aged AGR component and demonstrate high-resolution 2D and 3D representations for nondestructive diagnosis of the component. The tomography showed that the AGR component did not deform or suffer broken AGR channels. Closer analysis of the component's center revealed that the distribution of the particle accumulation in the middle of the top block was visibly heavier than the accumulation at the entrance and exit of the top block. The NCT data also revealed that the downstream block had much lower soot accumulation, which continued to gradually decrease farther downstream to the exit. Furthermore, the representative cross-sectional views at different locations revealed significant aggregation in the central region but not at the rim along the cylindrical cross section. The spatial details throughout the AGR component revealed by the 3D tomography provide unique and detailed information on the aged AGR by nondestructive means. This information can assist in the redesign of accessory parts and the specifications of monolithic channel sizes/shapes for AGR components to enable a uniform, self-cleaning flow patten and alleviate significant soot aggregation in any region of the AGR component.

One of the practical challenges for AGR technology is the reduction of precious metals. Expensive precious metals represent nearly 90% of the cost of the AGR component. Thus, a new AGR catalyst with low precious metal loading was preliminarily explored to identify a pathway of optimizing AGR material

loading and maximizing acidic gas reduction at low cost. The new AGR component developed can reduce precious metal loading by 38% and still achieve a neutral condensate and ultralow NOx emissions. The furnace with the AGR with low Pt/Rh loading enabled a maximum AFUE of 97%, which is meaningfully higher than the original furnace. Long-duration test for the furnace enabled with the low precious metal loading AGR component is vital in the future research.

The current work demonstrates a proof of concept for the AGR-enabled furnace, and the AGR assembly must be optimized and integrated into the design of new OEM furnace products. Furthermore, the AGR technology can be applied not only for residential gas furnaces, but also for commercial rooftop units, gas heat pumps, gas-fired water heaters, combustion boilers, and other systems.

ACKNOWLEDGMENTS
This work was sponsored by the U.S. DOE Building Technologies Office, with Antonio Bouza and Isaac Mahderekal as program managers. This research used resources at the Building Technologies Research and Integration Center, a DOE Office of Science User Facility operated by the Oak Ridge National Laboratory. We also thank Drs. Calvin Thomas and Lingshi Wang and many others who provided helps in testing.

REFERENCE

1. EIA. https://www.eia.gov/energyexplained/use-of-energy/homes.php; 2021 [accessed 2 August 2021].
2. Yang Z, Qu M, & Gluesenkamp KR. Design screening and analysis of gas-fired ammonia-based chemisorption heat pumps for space heating in cold climate. Energy 2020; *207*:118213. https://doi.org/10.1016/j.energy.2020.118213
3. Brodrick JR, Moore A. Conquering corrosion. ASHRAE journal 2000; 42(4):29-32. https://www.jstor.org/stable/45363418
4. Anonymous. Pipe-sweating from natural gas fires. Engineering Review 1901;1 1: Feb. p. 18.
5. AGA. https://www.aga.org/sites/default/files/2017_furnace_efficiency_rule.pdf; 2017 [accessed 2 August 2021].
6. Momen AM, Munk J, Hughes P. Condensing furnace venting part 2: evaluation of same-chimney vent systems for condensing furnaces and natural draft water heaters. ORNL/TM-2014/656, 2015.
7. Lutz J, Lekov A, Chan P, Whitehead CD, Meyers S, McMahon J. Life-cycle cost analysis of energy efficiency design options for residential furnaces and boilers. Energy 2006; 31(2-3):311-329. https://doi.org/10.1016/j.energy.2005.02.002
8. Lekov A., Franco V, Meyers S, McMahon JE, McNeil M, Lutz J. Electricity and Natural Gas Efficiency Improvements for Residential Gas Furnaces in the US, https://escholarship.org/uc/item/0pw5p1tq; 2006 [Accessed, 2 August 2021].
9. Wu P, Shang W, Chen J. Study of flow field of a residential gas furnace with particle image velocimetry. In ASME Fluids Engineering Division Summer Meeting (Vol. 51562, p. V002T11A018), 2018.
10. Tu Y, Liu H, Chen S, Liu Z, Zhao H, Zheng C. Effects of furnace chamber shape on the MILD combustion of natural gas. Applied Thermal Engineering 2015; 76: 64-75. https://doi.org/10.1016/j.applthermaleng.2014.11.007
11. Belosevic S, Paprika M, Komatina M, Stevanovic Z, Mladenovic R, Oka N, Dakic D. Experimental and numerical investigation of heat exchanger built in solid fuel household furnace of an original concept. Energy and Buildings 2005; 37(4):325-331. https://doi.org/10.1016/j.enbuild.2004.06.018
12. Yin P, Pate MB. Impact of duct flow resistance on residential heating and cooling energy use in systems with PSC and ECM blowers. Energy and Buildings 2016; 130: 625-636. https://doi.org/10.1016/j.enbuild.2016.08.012
13. Zhao Y, McDonell V, Samuelsen S. Assessment of the combustion performance of a room furnace operating on pipeline natural gas mixed with simulated biogas or hydrogen. International Journal of Hydrogen Energy 2020; 45(19):11368-11379. https://doi.org/10.1016/j.ijhydene.2020.02.071
14. Al Omari SA, Hamdan MO, Selim MY, Elnajjar E. Combustion of jojoba-oil/diesel blends in a small scale furnace. Renewable Energy 2019; 131:678-688. https://doi.org/10.1016/j.renene.2018.07.009
15. Jiru TE, Kaufman BG, Ileleji KE, Ess DR, Gibson HG, Maier DE. Testing the performance and compatibility of degummed soybean heating oil blends for use in residential furnaces. Fuel 2010; 89(1):105-113. https://doi.org/10.1016/j.fuel.2009.07.028
16. Chandrasekaran SR, Sharma BK, Hopke PK, Rajagopalan N. Combustion of switchgrass in biomass home heating systems: Emissions and ash behavior. Energy & Fuels 2016; 30(4):2958-2967. https://doi.org/10.1021/acs.energyfuels.5b02624

17. Kakareka SV, Kukharchyk TI, Khomich VS. Study of PAH emission from the solid fuels combustion in residential furnaces. Environmental pollution 2005; 133(2):383-387. https://doi.org/10.1016/j.envpol.2004.01.009

18. Tashtoush G, Al-Widyan MI, Al-Shyoukh AO. Combustion performance and emissions of ethyl ester of a waste vegetable oil in a water-cooled furnace. Applied thermal engineering 2003; 23(3):285-293. https://doi.org/10.1016/S1359-4311(02)00188-6

19. Addo–Binney B, Agelin-Chaab M, Bamfo E, Koohi-Fayegh S. A comparative life cycle assessment of a cascade heat pump and a natural gas furnace for residential heating purposes. Integrated Environmental Assessment and Management 2021. https://doi.org/10.1002/ieam.4494

20. Gluesenkamp KR, LaClair TJ, Cheekatamarla P, Abu-Heiba A. Self-powered Heating: Efficiency Analysis, In: International Refrigeration and Air Conditioning Conference, 2021. https://docs.lib.purdue.edu/cgi/viewcontent.cgi?article=3212&context=iracc

21. Abu-Heiba A, Gluesenkamp KR, LaClair TJ, Cheekatamarla P, Munk JD, Thomas J, Boudreaux P. Analysis of power conversion technology options for a self-powered furnace. Applied Thermal Engineering 2021; 188:116627. https://doi.org/10.1016/j.applthermaleng.2021.116627

22. Elias RS, Yuan M, Wahab MIM, Patel N. Quantifying saving and carbon emissions reduction by upgrading residential furnaces in Canada. Journal of Cleaner Production 2019; 211:1453-1462. https://doi.org/10.1016/j.jclepro.2018.11.214

23. Milcarek RJ, DeBiase VP, Ahn J. Investigation of startup, performance and cycling of a residential furnace integrated with micro-tubular flame-assisted fuel cells for micro-combined heat and power. Energy 2020; 196:117148. https://doi.org/10.1016/j.energy.2020.117148

24. Liberty. https://www.libertyplumbingheatingandair.com/california-new-furnace-emissions-standards/; 2021 [accessed 2 August 2021].

25. Gao Z, Chakravarthy K, Daw CS, Conklin J. Lean NOx trap modeling for vehicle systems simulations. SAE Int. J. Fuels Lubr. 2010; 3(1):468-485. https://doi.org/10.4271/2010-01-0882

26. Gao Z, Kim M-Y, Choi J-S, Daw C, Parks II J, Smith D. Cold-start emissions control in hybrid vehicles equipped with a passive hydrocarbon and NOx adsorber. Proc. IMechE–Part D: Journal of Automobile Engineering 2012; 226(10): 99-107. https://doi.org/10.1177/0954407012443764

27. Zhang Y, Ravi Chandran KS, Jagannathan M, Bilheux HZ, Bilheux JC. The nature of electrochemical delithiation of Li-mg alloy electrodes: neutron computed tomography and analytical modeling of Li diffusion and delithiation phenomenon. Journal of the Electrochemical Society 2016; 164:A28.

28. Zhang P, Wittmann FH, Zhao T, Lehmann EH. Neutron imaging of water penetration into cracked steel reinforced concrete. Physica B: Condensed Matter 2010; 405(7): 1866-1871.

29. Terreni J, Billeter E, Sambalova O, Liu X, Trottmann M, Sterzi A, et al. Hydrogen in methanol catalysts by neutron imaging. Physical Chemistry Chemical Physics 2020; 22(40):22979-22988.

30. Zhang Y, Ravi Chandran KS, Bilheux HZ. Imaging of the Li spatial distribution within V2O5 cathode in a coin cell by neutron computed tomography. Journal of Power Sources 2018; 376:125-130.

31. Strzelec A, Bilheux HZ, Finney CEA, Daw CS, Foster DE, Rutland CJ, et al. Neutron imaging of diesel particulate filters. SAE Technical Paper No.2009-01-2735, 2009.

32. Gruenzweig C, Mannes D, Schmid F, Rule R. Neutron Imaging: A Non-Destructive Testing Method to Investigate Canned Exhaust After-Treatment System Components for the Three Dimensional Soot, Ash, Urea and Coating Distributions. SAE Technical Paper No. 2016-01-0985, 2016.

33. Babu SK, Spernjak D, Mukundan R, Hussey DS, Jacobson DL, Chung HT, et al. Understanding water management in platinum group metal-free electrodes using neutron imaging. Journal of Power Sources 2020; 472: 228442.

34. Boillat P, Lehmann EH, Trtik P, Cochet M. Neutron imaging of fuel cells–Recent trends and future prospects. Current Opinion in Electrochemistry 2017; 5(1): 3-10.

35. Fumey B, Borgschulte A, Stoller S, Fricker R, Knechtle R, Kaestner A, et al. Enhanced gas-liquid absorption through natural convection studied by neutron imaging. International Journal of Heat and Mass Transfer 2022; 182: 121967.

36. Geoghegan P, Sharma V. Neutron imaging of a two-phase refrigerant flow. In ASME International Mechanical Engineering Congress and Exposition (Vol. 57502, p. V08BT10A052). American Society of Mechanical Engineers, 2015.

37. Kardjilov N, Manke I, Hilger A, Strobl M, Banhart J. Neutron imaging in materials science. Materials Today 2011; 14(6), 248-256.

38. Wissink ML, Chen Y, Frost MJ, Curran SJ, Rios O, Sims ZC, et.al. Operando measurement of lattice strain in internal combustion engine components by neutron diffraction. Proceedings of the National Academy of Sciences 2020, 117, 52:33061-33071.

39. Gao Z, Momen AM, Pihl JA, LaClair TJ, Shen B, Liu X, Gluesenkamp KR, Parks IJE, Gao P, Pawlowski AE, Nawaz K. Monolithic gas trap adsorber for high efficiency, cost effective, low-emission condensing furnace. U.S. Patent Application 17/232,274, 2021.

40. Zhang M, LaClair T, Wang L, Liu X, Gao Z, Momen AM, Gluesenkamp K. A numerical study on the energy performance of a novel furnace with acidic gas trap absorbers. In: ASME Heat Transfer Summer Conference (Vol. 83709, p. V001T09A001), 2020.

41. ANSI/ASHRAE. ANSI/ASHRAE 103-2017: method of testing for annual fuel utilization efficiency of residential central furnaces and boilers. 2017.

42. EPA. https://www.epa.gov/emc/method-8-sulfuric-acid-mist; 2020 [accessed 2 August 2021].

43. Gao Z. Advanced Adsorption technology for new high-efficiency natural-gas furnace at low cost. A project review meeting with DOE BTO sponsor, 2021.

44. Crow L, Robertson L, Bilheux H, Fleenor M, Iverson E, Tong X, et al. The CG1 instrument development test station at the high flux isotope reactor. Nuclear Instruments and Methods in Physics Research Section A: Accelerators, Spectrometers, Detectors and Associated Equipment 2011, 634:S71-S74.

45. Zhang Y, Bilheux J, Bilheux H, Lin J. An interactive web-based tool to guide the preparation of neutron imaging experiments at Oak Ridge National Laboratory. Journal of Physics Communications 2019; 3(10):103003.

46. Zhang Y, Bilheux J. ImagingReso: A Tool for Neutron Resonance Imaging. Journal of Open Source Software 2017; 2(19):407.

47. Kaestner AP. MuhRec A new tomography reconstructor, Nuclear Instruments and Methods in Physics Research Section A: Accelerators, Spectrometers, Detectors and Associated Equipment 2022; 651(1):156-160, doi:10.1016/j.nima.2011.01.129.

48. Stalling D, Westerhoff M, Hege H.-C. Amira: A Highly Interactive System for Visual Data Analysis. The Visualization Handbook 2005: 749–767. doi:10.1016/B978-012387582-2/50040-X.

49. Gao Z, Pihl J, LaClair T, Fricke B. Global kinetic modeling of NH_3-SCR with two sites of NH_3 storage on Cu-SSZ-13. Chemical Engineering Journal 2021; 406: 127120.

50. Liu J, Wu P, Sun P, Ji Q, Zhang Q, Wang P. Effects of iron-based fuel borne catalyst addition on combustion, in-cylinder soot distribution and exhaust emission characteristics in a common-rail diesel engine. Fuel 2021; 290:120096.

51. Ferrari AC, Robertson J. Raman spectroscopy of amorphous, nanostructured, diamond–like carbon, and nanodiamond. Philosophical Transactions of the Royal Society of London. Series A: Mathematical, Physical and Engineering Sciences 2004; 362 (1824): 2477-2512.

52. Gao Z, Gluesenkamp K, Gehl A, Pihl J, LaClair T, Zhang M, Sulejmanovic D, Jeffrey M, Nawaz K. Ultra-clean condensing gas furnace enabled with acidic gas reduction. Energy 2021, 243:123068.

53. Gao, Zhiming, Kyle R. Gluesenkamp, Dino Sulejmanovic, Tim Laclair, Anthony C. Gehl, Josh Pihl, et al. *Clean and High-Efficiency Natural Gas Furnace with Advanced Acidic Gas Trap Technology*. Oak Ridge National Laboratory, Oak Ridge, TN (United States), 2021.

APPENDIX A. PATENT, PUBLICATIONS AND MEDIA REPORTS

PATENT

- Gao Z, Momen AM, Pihl JA, LaClair TJ, Shen B, Liu X, Gluesenkamp KR, Parks IJE, Gao P, Pawlowski AE, Nawaz K. Monolithic gas trap adsorber for high efficiency, cost effective, low-emission condensing furnace. U.S. Patent Application 17/232,274, 2021.

PUBLICATIONS

- Z Gao, K Gluesenkamp, A Gehl, J Pihl, T LaClair, M Zhang, D Sulejmanovic, J Munk, K Nawaz. Ultra-clean condensing gas furnace enabled with acidic gas reduction. Energy 243 (2022): 123068.
- Z Gao, Y Zhang, S Qian, W Yang, Z Wu, K Gluesenkamp, K Nawaz. Nondestructive Neutron Image Diagnosis of Acidic Gas Reduction Catalyst After 400-Hour Operation in Natural Gas Furnace, Chemical Engineering Journal 2022, under review.
- Z Gao, KR Gluesenkamp, D Sulejmanovic, T Laclair, AC Gehl, J Pihl, M Zhang et al. Clean and High-Efficiency Natural Gas Furnace with Advanced Acidic Gas Trap Technology. ASHRAE 2021 Virtual Annual Conference, 2021.
- J Weng, P Gao, Z Gao, J Pihl, T LaClair, M Zhang, K Gluesenkamp, A Momen. Nanoarray-Based Monolithic Adsorbers for SO2 Removal. Emission Control Science and Technology 6(3) (2020): 315-323.
- M Zhang, T LaClair, L Wang, X Liu, Z Gao, AM Momen, K Gluesenkamp. A Numerical Study on the Energy Performance of a Novel Furnace with Acidic Gas Trap Absorbers. In Heat Transfer Summer Conference, Vol. 83709, p. V001T09A001. American Society of Mechanical Engineers, 2020.

MEDIA REPORTS AND PRESS RELEASES

- ASHRAE HVAC&R Industry News. Novel Solution Could Reduce Furnace Emissions. https://contentsharing.net/actions/email_web_version.cfm?ep=hDmEN8pY9mNWLxgFFXEk9oyLd2s6g38E40hIH0oyEc_zZhf_bz0CDLWIZCAgNDQOZwH0511zddh65b2wiT-eZM3vtwB6359uq_qL39ngBB_al9g58rjTDMJyZ5S8P6yx, March 2022
- DOE Science News Source. Buildings — Capturing furnace emissions. https://www.newswise.com/doescience/story-tips-beneath-the-skin-crustacean-inspired-cotton-automating-clean-water-samples-in-space-and-capturing-furnace-emissions/?article_id=766373, March 2022
- ORNL NEWS. Buildings – Capturing Furnace Emissions. https://www.ornl.gov/news/buildings-capturing-furnace-emissions, March 2022
- TECHNOLOGY.ORG: SCIENCE & TECHNOLOGY NEWS. Buildings – Capturing Furnace Emissions. https://www.technology.org/2022/03/02/buildings-capture-furnace-emissions/, 2022
- SOYLENT NEWS. Buildings — Capturing furnace emissions. https://soylentnews.org/article.pl?sid=22/03/03/1344253 , March 2022
- NEWSAXES. Researchers develop a approach to seize furnace emissions. https://newsaxes.com/researchers-develop-a-approach-to-seize-furnace-emissions/, March 2022.

APPENDIX A. FIGURES

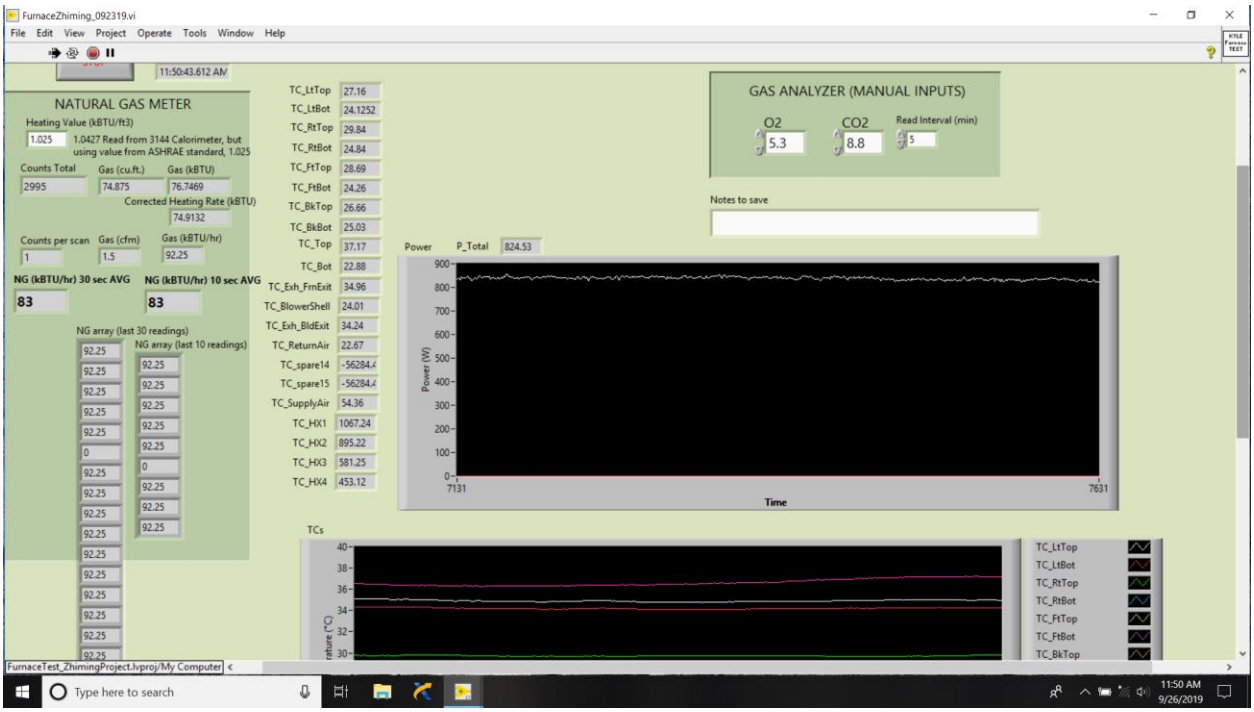

Figure A1. Data acquisition used in the furnace testing.

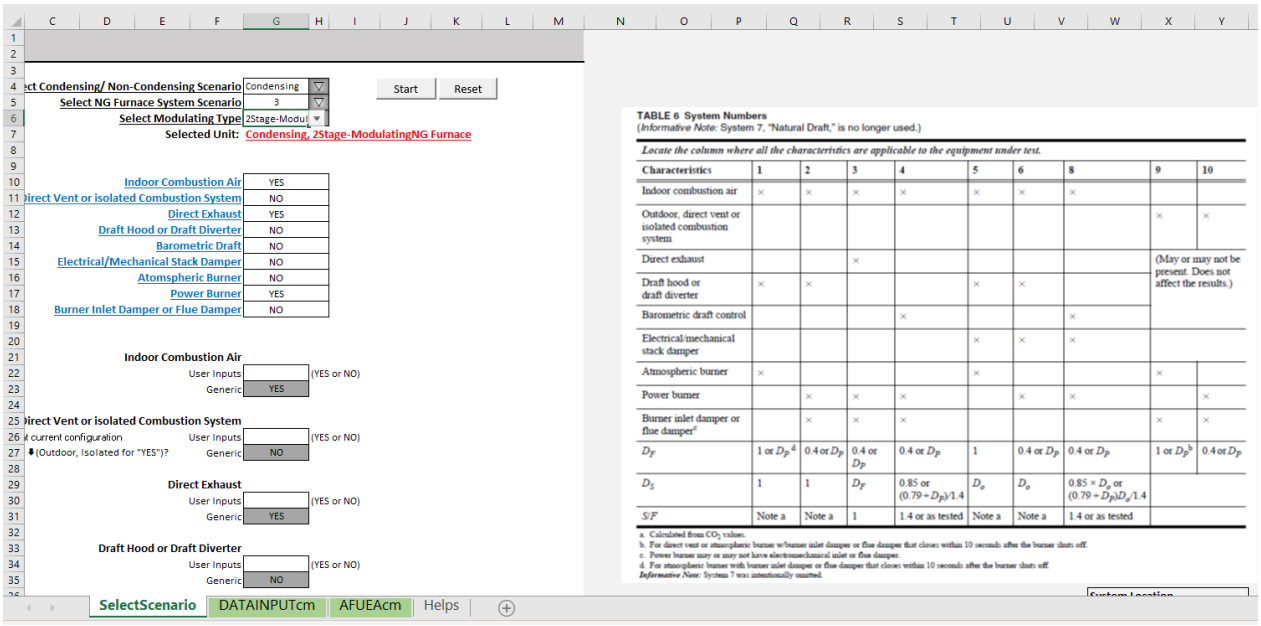

Figure A2: AFUE evaluation tool: the worksheet of unit and configuration selection.

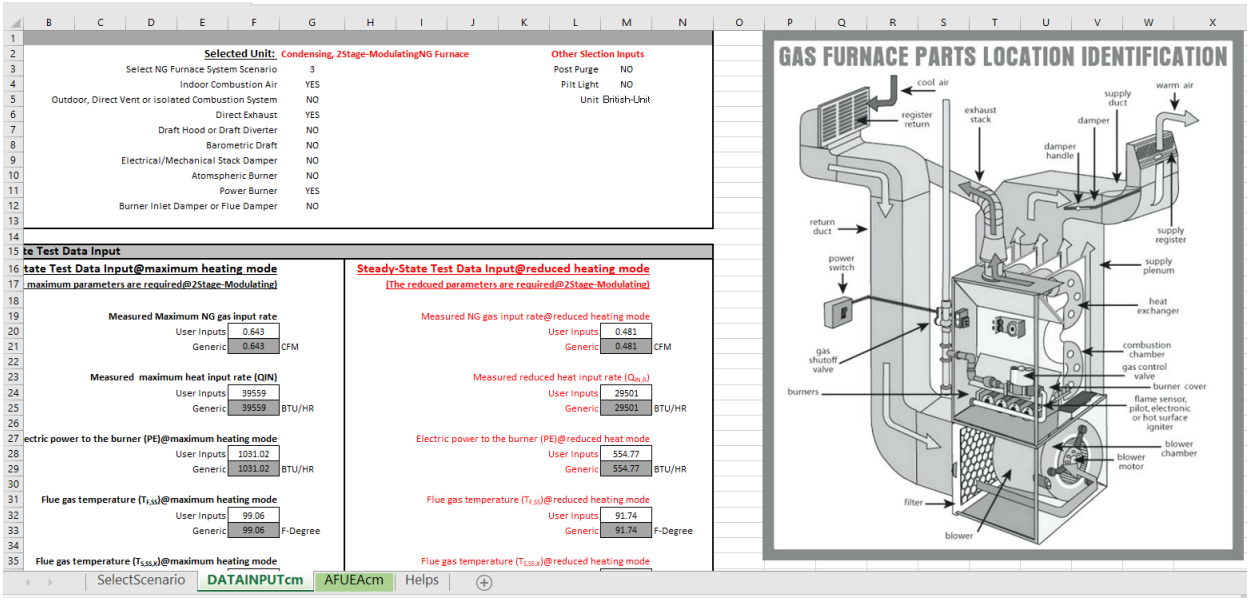

Figure A3: AFUE evaluation tool: the worksheet of geometry and measurement data input.

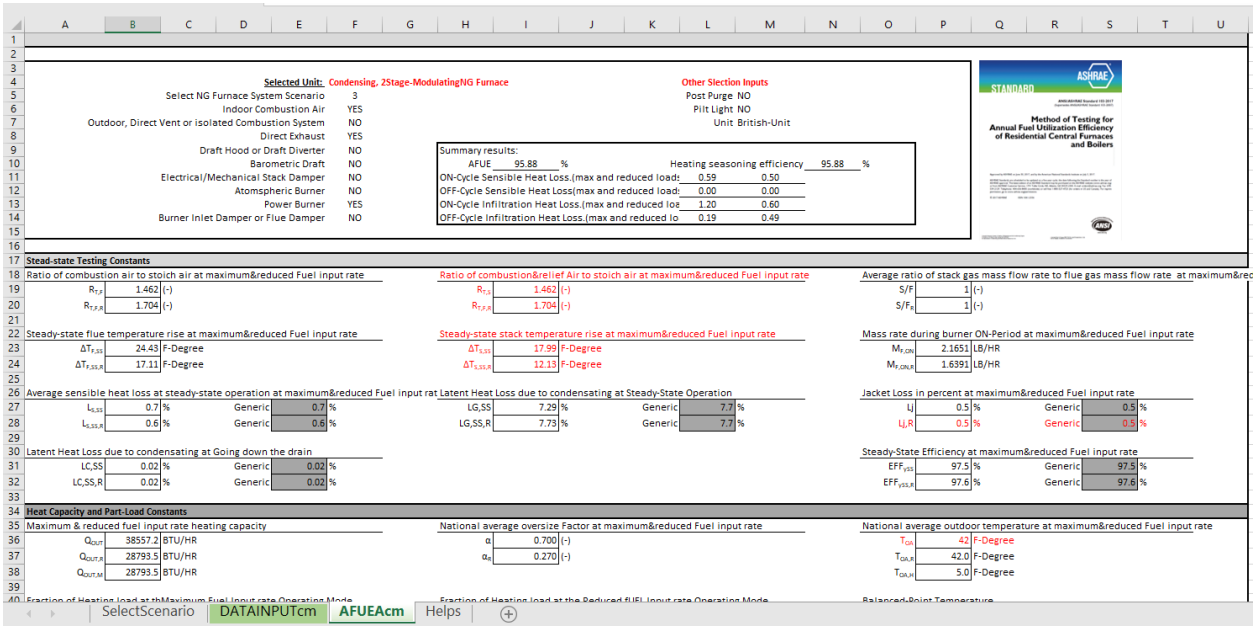

Figure A4: AFUE evaluation tool: the worksheet of AFUE and key results.